41/2-16-95 JS ①

PREPARED FOR THE U.S. DEPARTMENT OF ENERGY,
UNDER CONTRACT DE-AC02-76-CHO-3073

PPPL-2999
UC-420

PPPL-2999

ACTIVE CORE PROFILE AND TRANSPORT MODIFICATION BY APPLICATION OF ION BERNSTEIN WAVE POWER IN PBX-M

BY

B. LEBLANC, S. BATHA, R. BELL, ET AL.

JANUARY 1995

DISTRIBUTION OF THIS DOCUMENT IS UNLIMITED

PPPL PRINCETON PLASMA PHYSICS LABORATORY

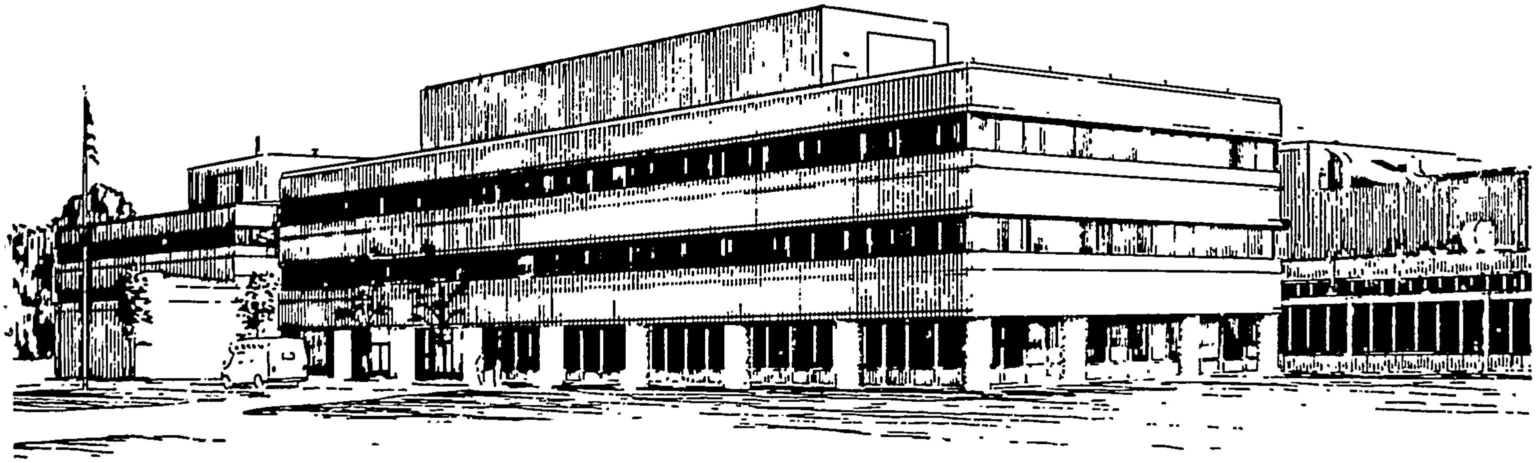

PRINCETON UNIVERSITY, PRINCETON, NEW JERSEY

NOTICE

This report was prepared as an account of work sponsored by an agency of the United States Government. Neither the United States Government nor any agency thereof, nor any of their employees, makes any warranty, express or implied, or assumes any legal liability or responsibility for the accuracy, completeness, or usefulness of any information, apparatus, product, or process disclosed, or represents that its use would not infringe privately owned rights. Reference herein to any specific commercial produce, process, or service by trade name, trademark, manufacturer, or otherwise, does not necessarily constitute or imply its endorsement, recommendation, or favoring by the United States Government or any agency thereof. The views and opinions of authors expressed herein do not necessarily state or reflect those of the United States Government or any agency thereof.

NOTICE

This report has been reproduced from the best available copy.
Available in paper copy and microfiche.

Number of pages in this report: 48

DOE and DOE contractors can obtain copies of this report from:

Office of Scientific and Technical Information
P.O. Box 62
Oak Ridge, TN 37831;
(615) 576-8401.

This report is publicly available from the:

National Technical Information Service
Department of Commerce
5285 Port Royal Road
Springfield, Virginia 22161
(703) 487-4650

Active Core Profile and Transport Modification by Application of Ion Bernstein Wave Power in PBX-M[#]

B. LeBlanc, S. Batha[d], R. Bell, S. Bernabei, L. Blush,[a] E. de la Luna,[b]
R. Doerner,[a] J. Dunlap,[c] A. England,[c] I. Garcia,[b] D. Ignat, R. Isler,[c] S. Jones,[f]
R. Kaita, S. Kaye, H. Kugel, F. Levinton,[d] S. Luckhardt,[f] T. Mutoh,[e]
M. Okabayashi, M. Ono, F. Paoletti,[f] S. Paul, G. Petravich,[g] A. Post-Zwicker,[c]
N. Sauthoff, L. Schmitz,[a] S. Sesnic, H. Takahashi, M. Talvard,[h] W. Tighe,
G. Tynan,[a] S. von Goeler, P. Woskov,[f] and A. Zolfaghari[f]

Princeton University, Plasma Physics Laboratory, Forrestal Campus,
P. O. Box 451, Princeton, NJ 08543

ABSTRACT

Application of Ion Bernstein Wave Heating (IBWH) into the Princeton Beta Experiment-Modification (PBX-M) [Phys. Fluids B **2**, 1271 (1990)] tokamak stabilizes sawtooth oscillations and generates peaked density profiles. A transport barrier, spatially correlated with the IBWH power deposition profile, is observed in the core of IBWH assisted neutral beam injection (NBI) discharges. A precursor to the fully developed barrier is seen in the soft x-ray data during edge localized mode (ELM) activity. Sustained IBWH operation is conducive to a regime where the barrier supports large ∇n_e, ∇T_e, ∇v_ϕ, and ∇T_i, delimiting the confinement zone. This regime is reminiscent of the H(high)-mode but with a confinement zone moved inwards. The core region has better than H-mode confinement while the peripheral region is L(low)-mode-like. The peaked profile enhances NBI core deposition and increases nuclear reactivity.

An increase in central T_i results from χ_i reduction (compared to H-mode) and better beam penetration. Bootstrap current fractions of up to 0.32-0.35 locally and 0.28 overall were obtained when an additional NBI burst is applied to this plasma.

[#] Paper 4I3, Bull. Am. Phys. Soc. **38**, 1959 (1993)

[a)]Deparment of Physics, University of California-Los Angeles, Plasma Physics Laboratory, 405 Hilgard Avenue, Los Angeles, California 90024-15

[b)]Centro de Investigaciones Energeticas Medioambientales y Technologicas, Avenida Complutense, 22; 28040-Madrid-España

[c)]Fusion Energy Division, Oak Ridge National Laboratory, P. O. Box 2009, Oak Ridge, Tennessee 37831-8072

[d)]Fusion Physics and Technology, 3547 Voyager Street, Suite 104, Torrance, California 90503-1673

[e)]National Institute for Fusion Science, Furo-cho, Chikusa-ku, Nagoya 464-01, Japan

[f)]Massachusetts Institute of Techonology, 77 Massachusetts Avenue, Cambridge, Massachusetts 02139

[g)]KFKI Research Institute for Particle and Nuclear Physics of the Hungarian Academy of Sciences, H-1525 Budapest, P.O. Box 49, Hungary

[h)]Département de Recherches sur la Fusion Controlée, Centre d'Etudes Nucléaires de Cadarache, F-13108 Saint-Paul-lez-Durance, France

I. INTRODUCTION

Active methods for profile control increase the chances of success of nuclear-fusion reactors based on the tokamak concept by extending plasma operations beyond the usual low (L-) and high (H-) modes to include more advanced high performance regimes. Progress in that direction has been made with the supershot[1] and pellet enhanced performance (PEP) mode[2] regimes, which make use of carefully orchestrated peaked density profiles. Plasma pressure control is an important issue for advanced tokamak regimes and is particularly crucial when considering high-β_p discharges with a large bootstrap current fraction. For example, by properly aligning the bootstrap current (or equivalently, the pressure profile) to insure stabilization of ballooning and kinetic modes, an attractive high performance regime with negative shear has been proposed.[3]

The application of localized auxiliary power through resonant deposition of radio-frequency (RF) power foretells attractive ways of profile control. In particular, a properly launched electron plasma wave transforms into an ion Bernstein wave (IBW) which can be absorbed resonantly in the plasma core.[4] The resonant nature of the process allows for some level of localization. This technique, used in the Princeton Beta Experiment-Modification[5,6] (PBX-M) to couple auxiliary power to the bulk ions, constitutes an important element of the profile control program; it is customarily referred to as "Ion Bernstein Wave Heating" or IBWH. Localized ion heating by IBWH has been observed in PBX-M and is reported elsewhere.[7]

Previous experimental results on Princeton Large Torus[8] (PLT) and *Alto-Campus-Torus-C*[9] (ALCATOR-C) have shown an increase of the global particle confinement[10,11] during IBWH. More recently, density peaking was reported[4,12,13] in the Japanese Institute of Plasma Physics Tokamak II-

Upgrade (JIPPII-U)[14] and PBX-M. The present paper is concerned with IBWH-assisted discharges, where neutral beam injection (NBI) delivers most of the heating power, and a relatively small amount of RF power (less than 23% of the input power) is used to modify locally the plasma profile and transport. In these discharges, density peaking is observed and plasma core heating is enhanced. The experimental data suggest the formation of an inner transport barrier, which coincides with the IBWH power deposition profile. Prior to the kinetic concretization of the barrier, but at the same position, a localized reduction of the soft-x-ray (SXR) loss during edge localized mode (ELM) events is observed. Sustained IBWH operation has been conducive to a regime of operation where most of the plasma energy is contained within the inner transport barrier, which then supports strong ∇n_e, ∇T_e, ∇v_ϕ, and ∇T_i. This condition, somewhat reminiscent of an H-mode, but with a transport barrier relocated inwards, has been phenomenologically termed the CH-mode (Core High confinement mode). Experimental data show an increase of central T_i and the neutron production rate during the CH-mode. Transport analyses indicate a reduction of transport of bulk ion energy and toroidal momentum, and low particle diffusion in the core region. Taking advantage of peaked pressure and strong density gradient of the CH-mode, bootstrap current fractions of up to 0.35 locally and 0.28 overall are obtained when an additional NBI burst is applied to a CH-mode target.

In the following, simultaneous operation of IBWH and NBI will be referred to as an IBWH-assisted discharge; NBI-only will stand for operation with NBI but without IBWH. The RF is launched from antennas located outboard of the magnetic axis and on the horizontal midplane. The IBWH power deposition profile is obtained from ray tracing calculation.

In Sec. II, we will give an overview of an IBWH-assisted discharge, and a comparison with a NBI-only discharge. Section III will present experimental observations in support of the formation of the inner transport barrier during IBWH-assisted discharges. Sec. IV will follow with a transport analysis of the CH-mode. Section V will address the plasma composition. An application of the profile control capability of IBWH for enhanced core heating will be discussed in Sec. VI, where the CH-mode is used as a target for additional NBI. A discussion is presented in Sec. VII and a conclusion follows.

II. IBWH IN AN H-MODE TARGET PLASMA: DENSITY PEAKING, SAWTOOTH AND ELM ELIMINATION

Figure 1 shows a comparison of the temporal evolution between two NBI discharges: one with a long IBWH pulse (black line) and one with a short pulse (gray line). IBWH and NBI power traces are shown in the bottom two panels. The following conditions are common to both discharges: NBI is applied from 0.35 to 0.7 s; flat top power is 2 MW. The plasma current I_p is 0.25 MA, the toroidal field is 1.5 T. The RF frequency is 55 MHz. The plasmas are mildly shaped with nominal parameters: elongation of 1.55, triangularity of 0.55, and indentation of 0.10. In the long RF pulse case, IBWH is applied from 0.46 to 0.68 s (next to bottom panel) and reaches a peak power of 0.3 MW at 0.5 s; this discharge illustrates IBWH-assisted operation. On the other hand, the short RF pulse does not reach full power and turns off after less than 0.04 s causing no significant effects: this discharge will be used as an example of NBI-only operation.

We can see (Fig.1, top panel) that, except for small discontinuities associated with MHD activity, the line integrated density, $n_e l$, for both discharges overlay closely. The IBWH-assisted discharge shown here does not correspond to the best IBWH-induced performance, and has been selected solely because of its good n_{el} match with the reference NBI-only discharge.

The second and third panels show the time evolution of the soft x-ray intensity, i.e., the chord-integrated signal from the center (I_{Xo}) and the mid minor radius ($I_{Xa/2}$). The interest of this data lies primarily in its high time resolution, which makes it suitable for MHD activity observation. Except for minor differences in the timing of sawtooth events, the temporal evolution of the soft x-ray traces agree well up to the 0.52 s time point when the two $I_{Xa/2}$ traces bifurcate: the IBWH-assisted trace begins a descent while the NBI-only trace remains high. Sawtoothing stops for times greater than 0.56 s during IBWH. The central soft x-ray intensities increase in unison until they separate at 0.575 s: the IBWH-assisted I_{Xo} pursues a sawtoothless ascent while the NBI-only I_{Xo} fluctuates around the same mean level, in response to MHD activity (sawteeth and ELMs). The peaking of the SXR profile is caused by the combined effects of a progressive n_e profile peaking, as will be seen below (Fig. 3), and also of impurity accumulation occurring after sawtooth elimination.

The upper-divertor-D_α traces (fourth panel in Fig. 1) show that both discharges entered the H-mode at $t_H \approx 0.42$ s, but the D_α temporal behavior differs shortly after the application of the RF pulse. With IBWH, the "DC" level of the D_α signal increases with time, and small ELM's appear from 0.53 s to 0.595 s. From the latter time on, ELM activity stops. The nature of the large D_α spike seen at ≈0.6 s is still under investigation, but it seems related to the loss of H-mode characteristics in the peripheral plasma.

The NBI-only discharge exhibits sawteeth from early times — the first large sawtooth is visible at 0.42 s — until the discharge termination. For times 0.53-0.585 s, we observe enhanced transport periods (ETP),[15] where the energy is lost primarily in the confinement region outside the $q=1$ surface. These periods of enhanced transport, characterized by bursts of small ELM-like events, can be observed as broad features in the D_α signal and a decrease in the $I_{a/2}$ signal: one between 0.53 and 0.57 s and the other between 0.57 and 0.585 s. The narrower features in the D_α signal after 0.59 s are large ELM's; they persist until end of NBI. The MHD activity observed during the NBI-only reference discharge is typical of H-modes with 2-MW NBI in PBX-M.

Figure 2 complements the data shown in Fig. 1 for the same two discharges. In the top panel, we can see the time evolution of the neutron source strength S_n. A drop of S_n is registered at the H-mode transition, followed by an increase which develops until 0.48 s when the neutron signals initiate a descent. As noted earlier, there is a good $n_e l$ match for these discharges and, remembering that the beam injection was kept the same, we observe that the S_n traces overlay well during the earlier times before IBWH effects on the profile become perceptible. While a monotonic decrease of S_n characterizes the NBI-only discharge (in gray), the IBWH-assisted (in black) discharge shows a reversal of the trend: for times 0.56-0.59 s the neutron signal levels off and increases for times greater than ≈0.595 s. This turnaround of the S_n temporal behavior was found to be a useful "control-room" indicator of the occurrence of the CH-mode. We will refer to the time at which S_n begins to increase (after leveling off) as t_{CH}; it marks the beginning of the CH-phase, see Fig. 2. This time also correlates well with the ELM activity termination and the D_α signal return to an L-mode signature. For times greater than 0.63 s during IBWH, S_n reaches saturation and is accompanied by either by a strong m=1/n=1 mode (20 kHz) or by simultaneously bursting, non propagating n=3, n=4, n=5 (60 to 100 kHz) modes observed in the soft x-ray data (not shown in Fig. 1). We will refer to this part of the CH-phase as the saturated or fully developed CH-mode.

The time evolution of the ion temperature echoes that of the neutrons. We can see in the second panel of Fig. 2, a plot of the central ion temperature, T_{io}, against time; T_{io} is measured by charge exchange recombination spectroscopy. This technique measures the ion temperature, T_i, and toroidal velocity, v_ϕ, of an impurity, which is oxygen in the present case. In the following, T_i and v_ϕ are assumed to be the bulk deuteron temperature and toroidal velocity. Similar to the observation made with S_n, the T_{io} temporal evolution agree for the earlier time interval 0.38-0.48 s. For times greater than 0.48 s, the NBI-only T_{io} decreases monotonically. In the IBWH-assisted case, T_{io} decreases faster during the 0.55-0.6 s interval but then recovers for times greater than ≈0.6 s (even though n_{eo} continues to rise, see Fig. 3(c)) and appears to saturate for times greater than 0.64 s.

The third panel shows the time evolution of the total stored energy, W_{tot}, obtained from transport analysis to be discussed below. Similarly to the observations made above, there is good agreement during the earlier times. At 0.53 s, the IBWH-assisted stored energy begins to drop faster than for the NBI-only discharge, but later starts a recovery at ≈0.6 s. In this particular discharge the W_{tot} recovery is modest, but we will see later (Fig. 9) that higher W_{tot} is feasible. It can be seen that the start of the recovery of S_n, *Tio, and* W_{tot} happen simultaneously at t_{CH}, bearing in mind (1) the size of the T_i data error bars and the 0.02 s integration time, (2) the temporal resolution of the transport analysis, which is on the order of 0.02 s. This time also corresponds to the cessation of ELM activity.

Density peaking has been observed with 51-spatial-point Thomson scattering measurements. The top panel in Fig. 3 presents overlays of electron density profiles, $n_e(R)$, against major radius R at four successive times during IBWH-assisted discharges; the $n_e(R)$ presented were smoothed to improve clarity. A typical error bar is shown. The data shown reflect a concatenation of single-time-point profile measurements from similar discharges, and show profiles obtained during the IBWH-assisted condition in Fig. 1; IBWH starts at 0.46 s. Referring to Fig. 1 will help in following the discussion of Fig. 3(a). Each profile has been labeled according to discharge phase. The 0.45 s profile (Early H-mode) was taken shortly after the L-H transition; the 0.5 s profile (H-mode) was taken during the H-mode phase when n_{el} increases but before density peaking; at 0.55 s (Peaked H-mode), density peaking has occurred but the plasma is still in the H-mode, as attested by the high edge density and the ELM activity (see Fig. 1); the 0.65 s profile corresponds to the condition introduced earlier as the CH-mode. Figure 3(b) shows the "peaking parameter" $n_{eo}/<n_e>$, where n_{eo} is the central electron density and $<n_e>$ is the volume-averaged density. The data correspond to IBWH-assisted discharges, and are derived from Thomson scattering measurements. The open points correspond to an IBWH-assisted discharge and the solid point corresponds to a NBI-only discharge. The vertical error bars are associated with the uncertainty in the determining the plasma edge. The horizontal error bars have been set to account for the discharge reproducibility. The peaking parameter, which hovers around 1.75 during the L-mode, falls to 1.4 during the H-mode and begins ascent up to 2.3 during the peaked H-mode; the ensuing CH-mode phase brings $n_{eo}/<n_e>$ up to 2.6. At 0.6 s, an NBI-only discharge has a peaking parameter of 1.6. A smoothed curve has been added. Fig. 3(c) presents a plot of T_{eo} against time. The open and solid squares correspond to Thomson scattering measurements; a smoothed curve has been added to help in the data visualization. A representative time evolution of n_{eo} is also shown. From the IBWH onset at 0.46 s to the end, T_{eo} falls by 30% while n_{eo} rises monotonically by a factor of two. The data suggest a small T_{eo} increase during the CH-mode (for times greater than 0.6 s).

III. EVIDENCE OF FORMATION OF A TRANSPORT BARRIER

Profile diagnostics offer experimental evidence of the formation of a transport barrier in the core region during the application of IBWH in NBI discharges.

A "kinetic" concretization of the barrier is observed after t_{CH}, and can be seen in the Thomson scattering data as illustrated in Fig. 4. The PBX-M TVTS[16] system provides $T_e(R)$ and $n_e(R)$ profiles with a spatial resolution of ≈1 cm; error bars are shown for some of the experimental points. Profiles associated with IBWH-assisted and NBI-only discharges are shown in black and gray respectively; measurements were made at the same times. In the top panel of Fig 4(a), overlays of T_e profiles are shown: the T_e profile measured during IBWH is higher and broader in the core region than that obtained during NBI-only operation. The top panel of Fig. 4(b) displays the corresponding n_e profiles In the IBWH-assisted case, the n_e profile is peaked with $n_{eo} = 0.96 \times 10^{14}/\mathrm{cm}^3$, while the NBI-only density profile is broad with $n_{eo} = 0.6 \times 10^{14}/\mathrm{cm}^3$. Corresponding ∇n_e and ∇T_e profiles are shown in the bottom panels. The ∇T_e profile during IBWH has large and localized maxima in the core region at a major radius R of ≈150 cm and ≈181 cm — ∇T_e reaches 100 eV/cm — which are not present in the NBI-only ∇T_e profile. Similarly, although with lesser localization, a large ∇n_e — up to $5 \times 10^{12}/\mathrm{cm}^4$ — exists in the core region of the IBWH-assisted plasma; these ∇n_e values are of the same magnitude as those obtained at the edge during NBI-only (H-mode). The confinement zone, where the large ∇n_e and ∇T_e are found, has been moved inward toward the core and away from the edge region. The data shown in Fig. 4 correspond to a CH-mode with $P_{IBWH} \approx 0.34$ MW and $P_{NBI} \approx 1.5$ MW.

Similar observations are made with the T_i and v_ϕ data. We can see in Fig. 5 the T_i and v_ϕ profiles measured at 0.64 s, ≈0.065 s after t_{CH}, in an IBWH-assisted discharge. Profiles for a NBI-only discharge, also taken at 0.64 s, are overlaid. It can be been that, while the H-mode has a peaked T_i profile, this profile during the CH-mode has a flat central region, at ≈1500 eV, which is slightly higher than for the H-mode and extends up to R=172 cm; it then falls rapidly below the H-mode level within 10 cm. Figure 5 also shows the associated gradient profiles in the lower panels. The CH-mode gradient peaks in the vicinity of R=179 cm, and at 140 eV/cm, it is three times larger than that of the H-mode. The CH-mode v_ϕ reaches 2.8×10^7 cm/s at the center, and is 20% larger than during the H-mode. For R>172 cm, the CH-mode v_ϕ falls below that of the H-mode. The CH-mode ∇v_ϕ also peaks in the vicinity of R=179 cm, where it is 3.5 times larger that the corresponding H-mode gradient, showing a qualitatively similar behavior as T_i.. The data shown in Fig. 5 correspond to a CH-mode with $P_{IBWH} \approx 0.3$ MW and $P_{NBI} \approx 2$ MW.

The effect of IBWH on the plasma can also be seen prior to t_{CH}, when the ELM activity attests to the localized action of IBWH. An array of 32 detectors fanning through the poloidal cross-section provides a vertical profile of the soft x-ray line integrated intensity. The energy loss experienced during an ELM can be studied by computing the difference between the soft x-ray intensity before and after the ELM: $\Delta I_X = I_{Xafter} - I_{Xbefore}$. Such ΔI_X profiles are shown in Fig. 6 for experimental conditions similar to those presented in Fig. 1. The ELM loss shown in the top panel is typical of an ELM occurring in an H-mode (NBI-only discharge in PBX-M): a large loss in the mid minor radius region with energy expelled to the edge region. The ELM behavior is modified by the application of

IBWH as illustrated in the bottom panel. The ΔI_X profile features localized minima (indicated by arrows). This characteristic, which has been observed only with IBWH, is indicative of a localized reduction of the ELM loss. The minima are localized $z \approx 16$ cm from the horizontal midplane, which corresponds to $r \approx 11$ cm from the magnetic axis when projected on an equatorial radial chord. These results show that under the action of IBWH, the SXR loss associated to an ELM event is reduced locally. The error ΔI_X bar of ± 0.02 μW is substantially smaller that the observed features. Although the energy loss is small ($\approx 1\%$), the instrumental sensitivity is sufficient to detect this change.

It will be shown below that the ∇n_e, ∇T_i, and ∇v_ϕ maximum positions coincide spatially with the energy loss minima observed in the SRX data during ELM activity and the IBWH power deposition profile.

IV. CORE PLASMA IMPROVEMENT: THE CH-MODE

As illustrated by the previous results, an improvement of the performance of the core plasma takes place during the CH-mode. One would like to ascertain whether these changes occur as a result of profile modification alone, or if confinement improvement is also involved. In order to answer this question, transport analyses were made using the TRANSP[17] code in a data reduction mode, where kinetic experimental profiles are inputted along with magnetically-determined plasma boundary and machine diagnostic data. A sophisticated atomic and nuclear model computes the fast-ion component.[18] Energy balance calculations are used to derive effective diffusivities: χ_i for the thermal ions, χ_ϕ for the toroidal rotation, and, χ_{er} for the combined electron transport including radiative losses. Instrumental problems preclude isolating the electron radial transport from radiation losses. Figure 7 shows the time evolution of χ_i, χ_ϕ, and χ_{er} against time. The data correspond to volume averages over $0.3 < r/a < 0.45$, in order to be representative of the plasma core. Auxiliary heating, NBI and IBWH, is also shown. The χ_i and χ_ϕ both show a substantial reduction at the time of the H-mode transition, while χ_{er} remains unchanged. A second drop of χ_i and χ_ϕ is visible during the CH-phase. The ion thermal diffusivity drops from $\approx$ 4.5 m^2/s during the L-mode to $\approx$ 2.5 m^2/s during the H-mode and subsequently down to $\approx$ 1 m^2/s during the CH-mode. The large χ_ϕ values during the early L-phase reflect a flat v_ϕ profile. The χ_{er} is not affected either by the H-mode, or the CH-mode. The error bar shown comes from an error analysis made with the same set of diagnostics on an operationally similar plasma.[19]

In regards to the particle transport, it is reasonable to assume that fueling in the core region of the CH-mode is dominated by NBI effects. An estimate of the electron particle diffusivity, D_e, based on this assumption is shown in Fig. 8. This calculation is valid for the core region, but underestimates D_e in the peripheral region since it neglects wall fueling. The plot corresponds to the 0.65 s time point in Fig. 7, and covers the inner 80% of the minor radius. The D_e trace has a minimum of $\approx 0.04\,m^2/s$ in the core region and increases for $r \geq 11$ cm. The D_e *(1×Ware)* trace corresponds to a similar computation but with the Ware pinch[20] velocity folded in; $D_e \approx 0.06\,m^2/s$ in the core. Wall fueling increases D_e in the peripheral region; an estimate of this effect is shown with shaded areas in Fig. 8. The particle diffusivity obtained in the core is small ($D_e/\chi_i \approx 1/20$), and one may wonder if some other effect comes into play. An anomalous inward pinch would increase D_e; for example, if one assumes an inward pinch five times greater than the Ware velocity, one gets $D_e \approx 0.16\,m^2/s$. Although the recycling increases during the CH-mode (D_α increases by $\approx$50% compared to the NBI-only discharge), edge effects are not thought to be important in core fueling.

V. PLASMA COMPOSITION

Spectroscopic analysis indicates that the IBWH power increases the influx of low Z and metallic impurities, e.g., iron and nickel. It appears that plasma-facing side of the stabilizing shell (stainless-steel) constitutes the source of these impurities, since the material of the Faraday shields is carbon or titanium carbide, and the inner pusher coil armor is made of carbon. During IBWH, the plasma emissivity profile peaks, and the total power radiated becomes of the order of the electron heating power (0.7-0.8 MW). Therefore, the electron power balance is expected to be dominated by radiative loss rather than conduction during the CH-mode. It is believed that a metallic impurity build-up in the plasma core, resulting from the increased influx, improved core confinement and high core density, dominates the radiation process. This would explain why T_{eo} remains clamped — or barely increases — during the CH-mode as seen in Fig. 3(c). A spectroscopic study[21] was made on IBWH-assisted discharges exhibiting poor CH-mode phase. In this case the metal concentration can reach up to 0.3% (of n_e). Although this is probably an upper limit, attempts have been made to incorporate the latter information into the plasma composition modeling. A limitation exists in the TRANSP constraint of only one impurity specie. The plasma composition is then determined by the Z_{eff} parameter and Z_I, the atomic number of the impurity.

The Z_{eff} fed into the analysis can be obtained from (1) a visible continuum measurement, $Z_{eff}(VC)$, or (2) the solution of the magnetic diffusion equation solved in a manner consistent with the measured loop voltage, $Z_{eff}(V_{sur})$. The measured $Z_{eff}(VC)$ corresponds to the plasma center and the profile is assumed flat. For the 0.35-0.66 s time interval, it was found that $Z_{eff}(VC) \leq Z_{eff}(V_{sur}) \approx 3.5$; during the CH-mode $Z_{eff}(V_{sur}) \approx Z_{eff}(VC) \approx 3.5$.

In the transport analyses it is assumed that up to 0.5 s the impurity is carbon ($Z_I = 6$), and that, under the influence of the metallic impurity influx, Z_I increases linearly up to 8 at 0.65 s and remains at this level for the rest of the discharge. This assumption gives a fuel fraction, n_D/n_e, of 0.5 at 0.5 s, and 0.64 at 0.65 s. The latter corresponds to impurity mix of 5% of fully stripped carbon and 0.3% of a metal with an effective charge of 19. Here, n_D is the deuteron density. In addition, some analyses have been made with a constant Z_I set to 6, in order to establish a baseline case without the effects of metallic impurities.

In order to judge the validity of the transport analysis, one can compare measured parameters like W_{tot}, the total stored energy, and S_n to the computation made by TRANSP of these quantities. Figure 9 displays W_{tot} and S_n vs. time in the top and the bottom panels, respectively. Three different analyses are presented. The bold solid line corresponds to an analysis using $Z_{eff}(V_{sur})$ and a variable Z_I as mentioned above. The thin solid line correspond to a similar analysis, but using $Z_{eff}(VC)$ instead. For the data shown as a dotted line, $Z_{eff}(V_{sur})$ was used with Z_I=6 during the whole discharge duration, which corresponds to an analysis assuming no metallic impurity accumulation. These analyses correspond to an IBWH-assisted discharge similar to what is shown in Fig. 1, but with better performance. It can be seen that in this case $t_{CH} \approx 0.56$ s, and that W_{tot} and S_n reach higher values than in Fig. 2. In the W_{tot} plot, values of the stored energy derived from magnetic measurements and computed by the equilibrium solver FQ[22] are shown. It can been seen that a reasonable agreement exists between TRANSP's W_{tot} outputs and FQ, although the Z_I=6 only analysis gives a slightly lower stored energy. For comparison, a TRANSP analysis was made for a NBI-only (H-mode) discharge, which corresponds to the NBI-only discharge shown in Fig. 1. In this analysis, $Z_{eff}(V_{sur})$ was used and Z_I=6. The kinetic documentation was not as complete as for the IBWH-assisted case, but it is believed to give a good representation of the time evolution of the stored energy.

In the bottom panel, the gray "EXP" trace corresponds to the measured neutron source strength. The S_n experimental error bar is ±15%.[23] The three analyses are displayed with the same line convention as above. There is agreement between the temporal behavior of the S_n computed by TRANSP and the measurement, although TRANSP overestimates it by 20% on average when $Z_{eff}(V_{sur})$ is assumed. This disagreement could be systematic. The TRANSP prediction overestimates S_n by 60% for the earlier times when using Z_{eff}(VC). The early-time S_n discrepancy has not been investigated thoroughly, but it could be explained by two causes: (1) anomalous fast-ion losses not included in the present TRANSP computation, which would greatly affect S_n since most of the neutrons come from beam-target reactions in these discharges; (2) the visible continuum inversion, which could be made problematic due to the absence of adequate viewing dumps and the presence of a NBI duct in the spectrometer line of sight. The analysis made with Z_I=6 gives a closer fit to the experimental data during the CH-mode, but does not account for the spectroscopic observations mentioned above. For comparison, the experimental NBI-only S_n is shown in the bottom panel. The CH-mode has a larger W_{tot} and S_n that the corresponding H-mode discharge. The diffusivivity curves shown in Fig. 7 corresponds to the "$Z_{eff}(V_{sur})$ with variable Z_I" analysis.

VI. ENHANCED CORE HEATING

The active profile and transport control capabilities of IBWH can be used to enhance plasma performance. The CH-mode plasma, with its peaked profile, allows deep penetration of the neutral beams, ensuring enhanced power deposition in the plasma core. On the other hand, one may wonder about the resilience of the CH-mode confinement when submitted to additional auxiliary power. An experiment was set up to examine this issue, where an additional 1.8 MW of NBI power was injected at the beginning of the CH-phase. The auxiliary-heating time history is shown in Fig. 10's top panel. The black traces correspond to IBWH-assisted operation; the gray trace corresponds to a reference NBI-only discharge with the same neutral beam power. The beginning of the discharge is kept the same as described above: initial NBI starts at 0.35 s; IBWH starts at 0.46 s and brings the discharge into the CH regime. Supplementary NBI is added in two steps at 0.55 s and 0.575 s; this "NBI burst" is made to correspond to the nominal onset of the CH-mode.

The bottom panel of Fig. 10 shows the S_n temporal behavior: the IBWH-assisted case is shown in black, and the NBI-only discharge is in gray. Although the S_n traces do not superimpose exactly during the earlier times, one can see that they match at 0.55 s, at the moment of the onset of the NBI burst. The IBWH-assisted discharge achieves a maximum neutron production rate of $\approx 2.6 \times 10^{13}$ s^{-1}, while the reference NBI-only discharge saturates at $\approx 1.6 \times 10^{13}$ s^{-1}. The application of a modest amount of IBWH power, less than 10% of the input power, has increased the neutron production rate by 60%. Although two isolated sawteeth at the beginning of the core heating phase are visible around 0.6 s, the IBWH-assisted discharge maintains its CH-mode character as seen in the S_n enhancement.

The IBWH-assisted and NBI-only discharges differ in the MHD activity observed during the S_n saturation phase. In the IBWH-assisted discharge, MHD modes in the 20-300 kHz range, with different n numbers, are observed with the SXR imaging system; similar observations are also made with a multichannel third harmonic cyclotron emission diagnostic.[24] The 20 kHz signal corresponds to an $m=1/n=1$ mode. In addition to this mode (and often in its absence), 60 kHz/$n=3$, 80 kHz/$n=4$, 100 kHz/$n=5$, and 120 kHz/$n=6$ modes are observed. Although these modes always have a strong component on the $q=1$ surface, they are more broadly localized modes on magnetic surfaces outside the $q=1$ surface: presumably 4/3, 5/4, etc. modes. They are all in a harmonic relationship with the $m=1/n=1$ mode, and are all non-propagating modes. The best match to the W_{tot} and S_n was obtained when using the $Z_I = 6$ impurity modeling. This observation is consistent with a dilution of the metallic impurity content caused by the NBI burst. On the other hand the S_n saturation for times greater than 0.63 s is not reproduced by TRANSP. During the S_n saturation phase of the NBI-only discharge, high frequency oscillations between 150 and 300 kHz have been seen.

Of particular interest is the bootstrap current generation during enhanced core heating. We can see in the top panel of Fig. 11 a plot of the TRANSP time evolution of the ratio of bootstrap current density, j_{BS}, to the (total) current density, j, at $r/a=1/2$. The bootstrap-current density fraction reaches 32% to 35% at $\approx$0.64 s depending on the impurity modeling, the higher value being obtained with Z_I variable as described above and the lower one obtained with constant Z_I; at that time the bootstrap current constitutes 28% of the total plasma current (250kA). The bottom panel of Fig. 11 shows profiles of j_{BS}, j_{BD} (the beam driven current density), and j against minor radius at 0.64 s. A broad j profile is obtained in the core region mainly because of the presence of a large bootstrap current in the high density gradient region near of $r/a=1/2$.

A TRANSP analysis was made to ascertain the confinement during enhanced core heating. We can see in Fig. 12, similar to Fig. 7, a plot of χ_{i}, χ_{ϕ}, and χ_{er} against time. The diffusivities are volume averaged over $0.3 < r/a < 0.45$. The discharge enters the H-mode at $\approx$0.45 s; the CH-mode onset occurs at ≈0.55 s. The auxiliary P_{NBI} and P_{IBWH} powers can be read on the right-hand vertical axis. The χ_i and χ_ϕ traces show a decrease for times greater than 0.55 s. The ion effective diffusivity decreases to slightly more than 1 m^2/s; this χ_i value is similar to that obtained during a CH-mode in the absence of the NBI burst, and is lower than that obtained during the H-phase. The fact that the H-mode transition is poorly resolved could due to the occurrence of a sawtooth at 0.415 s.

VII. DISCUSSION

A. IBWH-Induced transport barrier

While an absolute confirmation is not presently available, the data suggest that the inner transport barrier is of RF origin. Manifestations of the transport barrier, seen in the soft x-ray and kinetic data, coincide spatially with the IBWH power deposition profile. We can see in Fig. 13 overlays of gradient profiles ∇T_e, ∇n_e, ∇T_i, and ∇v_ϕ along with flux-surface mapping of the ion-absorbed IBWH power deposition P_{IBWH}. These profiles correspond to a well-developed CH-mode, and have been mapped over a single grid. Some level of smoothing is involved which flattens spatial features: while radial locations remain unchanged, the actual gradients may be larger. A spatial overlay exists between the P_{IBWH}, ∇T_i, ∇v_ϕ, and ∇n_e maxima. The ∇T_e profile peaks slightly more outside — by ≈3 cm — but nevertheless overlaps well with P_{IBWH}. Figure 13 shows arrows associated with the locations of the ΔI_X minima as projected on the major radius. This projection process and the absence of Abel inversion of the SXR data induce an error of ≈ 3 cm. Within the experimental spatial resolution, the ΔI_X minima and the locations of the maxima of ∇T_i, ∇v_ϕ, ∇n_e and P_{IBWH} are in agreement. The fact that the ∇T_e maximum location is slightly outside the ∇n_e ∇v_ϕ, and ∇T_i maxima could be caused by (1) T_e within the inner barrier being clamped by radiation losses, and hence preventing ∇T_e from developing fully, or (2) ∇T_e being influenced by the q=3/2 surface.

The transport barrier creation hypothesis is presently under study. A promising paradigm of IBWH-induced sheared-flow drive has been proposed,[25] which utilizes the unique conditions that can be set up in the plasma core by IBWH. When choosing a resonant layer on the lower field side of the magnetic axis, a traveling wave is generated which is absorbed before reaching the magnetic axis; this wave has a substantial radial electric field component, at right angles to the magnetic field, and a short wavelength of the order of ρ_i. These IBW properties give rise to efficient generation of sheared poloidal flow by ponderomotive action; shear flow levels thought to be sufficient to stabilize electrostatic turbulence can be achieved. The ponderomotive force is nonlinear in origin, and the fraction of the IBWH power rerouted for flow drive is small. The sheared flow is driven locally in the vicinity of the ion resonance layer. The physics of the turbulence suppression invoked here is the same as that of the L-H transition,[26] with the important distinctions that the transport barrier is externally induced, and its location is determined by the resonance layer.

The action of the inner barrier appears to have an important role in the development of the IBWH-assisted discharges. In the IBWH-assisted discharges described above, IBWH starts after the L-H transition. The power required to raise the inner barrier — about 300 kW for PBX-M parameters — is reached at 0.5 s and signs of its action become felt shortly afterward. Particles deposited within the barrier are better confined, initiating density peaking which becomes visible in the SXR data shortly after 0.525 s. The sawtooth elimination — from 0.56 s onward — could be the result of a modification of the current profile brought about by the rise in central density.

The CH-mode occurs when the confinement zone moves from the edge region to RF-induced inner barrier. The ensuing development appears to happens smoothly, within a time frame (≈0.045 s) or on the order of a few confinement times ($\tau_E \approx 0.02$-0.025 s), and starts at the recovery time. Experimental indicators of the confinement regime change are (1) the elimination of the ELM activity, which also indicates that the peripheral plasma is no longer in the H-mode; (2) S_n recovery; (3) T_{io} recovery; (4) W_{tot} recovery, (5) the appearance of the inner barrier in the kinetic data (∇T_e, ∇n_e, ∇v_ϕ, and ∇T_i). A transport barrier still exists at the edge, but it no longer supports the main gradients; the density inside the outer barrier falls during the CH-mode. This strong peaking appears to be non-transient in nature, since its duration is limited, so far, by the auxiliary heating system availability. Kinetic analysis indicates that during the neutron saturation phase of the CH-mode, up to 60% of the stored energy is contained in the core (within r=a/2); in PBX-M high-β_p discharges this ratio is ≈45%. The core ion diffusivity during the CH-mode is lower than the χ_i obtained during the H-mode phase of the discharge. The fact that χ_{er} does not drop during the CH-phase as seen for χ_i and χ_ϕ is most likely caused by the radiation losses.

The steep gradients induced during the CH-mode can generate, depending on the plasma collisionality, substantial bootstrap current in the vicinity of the inner barrier. This capability can be used to modify the current density profile as we have seen in Sect. V. Perhaps more importantly, by moving the confinement zone inwards, the bootstrap currents have been removed from the edge region, where it is known to trigger unwanted MHD instabilities including the external kink.

B. Impurities

The fact that a low Z_I value (Z_I=6-8) reproduces well W_{tot} and S_n suggests that the metallic impurities do not play a dominant role, except for the electron power balance. The choice of carbon as the resident impurity is warranted by the internal structure of PBX-M; rail limiters installed on the passive plates and the indentation coil armor are made of this element. The density of metallic impurities appear to be large enough to clamp the electron temperature through radiative processes, but not high enough to trigger a thermal collapse. Reduction of the impurity build-up would render these plasma more attractive by reducing the radiation losses. The success of the last IBWH campaign is thought to be partially due to in-situ probe boronization. More complete wall borinization is expected to further improve the performance of these plasmas.

At the present level of the analysis, the results presented in this paper are believed to differ from other density peaking results obtained in medium size tokamaks. The Z-mode[27] observed in ISX[28] is a low-Z impurity effect that enhances confinement through the electron channel, while in the CH-mode case the improvement is seen through the ions channel. Recent results on TEXTOR[29] show density peaking when silicon[30] is applied to walls. In these plasma, the radiation is located in the periphery and trend toward centrally peaked radiation is not observed, contrary the observation in the CH-mode.

C. Neutron strength enhancement

In PBX-M, after the initial turn-on phase of the neutral beam injection, most of the neutron production comes from beam-target reactions. The S_n increase observed during the CH-mode is principally caused by profile peaking of the target density. Using the discharge featured in Fig. 9, one finds this effect to contribute a ≈25% increases to S_n. The increase of the fuel fraction thought to be due to the replacement of low-Z impurity by higher-Z metallic impurity adds another ≈15% to S_n. The beam-target reaction rate being proportional to the fast-ion slowing-down time, the ≈7% T_e increment during CH-mode is responsible for another ≈10% increase of S_n. Finally, it is interesting to note that the thermonuclear fraction to S_n, which had been negligible <1%, rises to ≈3% during the CH-mode.

The S_n saturation observed during the enhanced core heating experiment, could be caused by the fast MHD activity which is observed simultaneously. Indeed TRANSP, which did not model anomalous fast-ion losses fail to reproduce this phenomenon.

D. Reactor relevance of IBWH

The utilization of RF-based methods for active control in a nuclear fusion reactor is attractive in view of its established technology and its compactness. The resonant nature of IBWH enables localized intervention of the plasma transport. The confinement zone can be moved to an operationally safer location away from the edge. The ensuing density peaking increases the nuclear reactivity with same stored energy or average beta, which may be limited by the beta-limit. The localized generation of bootstrap current can also be used to tailor the current density profile. Because of its profile control capabilities, IBWH could have substantial impact on the design of advanced tokamak based on self-supporting bootstrap current.

VIII. CONCLUSION

Desirable density peaking is readily achievable with IBWH-assisted operation. Experimental indicators and transport analyses show that the plasma core has good high confinement. The results are consistent with the generation of an RF-induced transport barrier located in the core region. This barrier, visualized in the earlier times by the SXR analysis of the ELM behavior, eventually defines and maintains the confinement zone. The latter stage can be seen in the various kinetic profile measurements and the attainment of the CH-mode. The fully-developed CH-mode is characterized by (1) an inner transport barrier supporting strong gradients of the kinetic variables ∇T_e, ∇n_e, ∇v_ϕ, and ∇T_i; (2) a peaked density profile; (3) sawtooth stabilization; (4) high core confinement; (5) edge region with L-mode like confinement, and without steep gradients or ELM's. The CH-mode is resilient to auxiliary heating. Substantial generation of localized bootstrap currents in the vicinity of the inner transport barrier is obtainable by lowering collisionality. While no direct confirmation is available at this time, the experimental data suggest that the inner barrier is RF-generated.

The utilization of IBWH has promising implications for advanced tokamaks by providing peaked density profiles for improved reactivity, and by introducing some degree of control of bootstrap current profile for increased high-β stability. The prospect of actively creating a transport barrier at desired radial location in the plasma through IBWH opens new areas of operation for magnetic confinement with tokamaks.

ACKNOWLEDGMENTS

This work is made possible through the diligent work of the many people of PPPL who provided technical, computer, and engineering support. This work is supported by United States Department of Energy Contract No. DE-AC02-76-CHO-3073

---

[1] D. Meade, V. Arunasalam, C.W. Barnes, M.G. Bell, R. Bell, M. Bitter, R. Boivin, N.L. Bretz, R. Budny, C.E. Bush, A. Cavallo, C.Z. Cheng, T.K. Chu, S.A. Cohen, S. Cowley, S.L. Davis, D.L. Dimock, J. Dooling, H.F. Dylla, P.C. Efthimion, A.B. Ehrhardt, R.J. Fonck, E.D. Fredrickson, H.P. Furth, R.J. Golston, G.J. Green, B. Grek, L.R. Grisham, G.W. Hammett, R.J. Hawrykuk, K.W. Hill, J.C. Hosea, R.B. Howell, H. Hsuan, R.A. Hulse, A.C. Janos, D.L. Jassby, F.C. Jobes, D.W. Johnson, L.C. Johnson, R. Kaita, S.M. Kaye, J. Kesner, C. Kieras-Phillips, S.J. Kilpatrick, H. Kugel, P.L. Lamarche, B. LeBlanc, D.M. Manos, D.K. Mansfield, E.S. Marmar, M.E. Mauel, E. Mazzucato, M.P. McCarthy, D.C. McCune, K.M. McGuire, S.S. Medley, D.R. Mikkelsen, D.A. Monticello, R.W. Motley, D. Mueller, J. Murphy, Y. Nagayama, G.A. Navratil, R. Nazikian, D.K. Owens, H.K. Park, W. Park, S.F. Paul, R. Perkins, S. Pitcher, A.T. Ramsey, M.H. Redi, G. Rewoldt, D.R. Roberts, A.L. Roquemore, P.H. Rutherford, S.A. Sabbagh, G. Schilling, J. Schivell, G.L. Schmidt, S.D. Scott, J. Snipes, J.E. Stevens, W. Stodiek, B.C. Stratton, E.J. Synakowski, W.M. Tang, G. Taylor, J.L. Terry, J.R. Timberlake, H.H. Towner, M. Ulrickson, S. von Goeler, R.M. Wieland, M. Williams, J.R. Wilson, K.L. Wong, M. Yamada, S. Yoshikawa, K.M. Young, M.C. Zarnstorff, S.J. Zweben, *Plasma Physics and Controlled Nuclear Fusion Research, 1990*, (International Atomic Energy Agency, Vienna, 1991), Vol. 1, p. 9.

[2] The JET Team, in Plasma Physics and Controlled Nuclear Fusion Research **1**, 215 (1989).

[3] C. Kessel, J. Manickam, G. Rewoldt, and W.M. Tang, Phys. Rev. Lett. **72**, 1212 (1994).

[4] M. Ono, Phys. Fluids B **5**, 241 (1993).

---

[5] R. E. Bell, N. Asakura, S. Bernabei, M. S. Chance, P.-A. Duperrex, R. J. Fonck, G. M. Gammel, G. Green, R. E. Hatcher, C. E. Kessel, H. W. Kugel, B. LeBlanc, F. M. Levinton, M. Okabayashi, M. Ono, S. F. Paul, E. T. Powell, Y. Qin, D. W. Roberts, N. R. Sauthoff, S. Sesnic, and H. Takahashi, Phys. Fluids B **2**, 1271 (1990).

[6] S. Bernabei, R. Bell, M.Chance, T.K. Chu, M. Corneliussen, W. Davis, G. Gettelfinger, T. Gibeny, N. Greenough, R. Hacher, H. Hermann, D. Igant, S. Jardin, R. Kaita, S. Kaye, C. Kessel, T. Kozub, H. Kugel, L. Largin, B. LeBlanc, J. Manickam, M. Okabayashi, H. Olivier, M. Ono, S. Paul, S. Preische, P. Roney, N. Sauthoff, S. Schweitzer, S. Sesnic, Y. Sun, H. Takahashi, W. Tighe, E. Valeo, S. von Goeler, K. Voss, M. Mauel, G. Navratil, R. Cesario, B. Batha, F. Levinton, F. Rimini, N Asakura, S. Jones, J. Kesner, S. Luckhardt, F. Paoletti, A Zolfaghari, T. Seki, J. Bell, J. Dunlap, A. England, D. Greewood, J. Harris, G. Henkel, S. Hischman, R. Isler, D. Lee, L. Blush, R. Conn, R. Doerner, Y. Hirooka, R. Lehmer, L. Schmitz, G. Tynan, Phys. Fluids. B **5** 2562 (1993)

[7] W. Tighe, R. Bell, T.K. Chu, H. Hermann, B. LeBlanc, M. Okabayashi, M. Ono, N. Asakura, R. Cesario, A. England, R. Isler, R. Kaita, H. Kugel, S. Paul, A. Post-Zwicker, H. Takahasi, *10th Topical Conference on Radio Frequency Power in Plasmas, Boston, MA, 1993,* edited by M. Porkolab and J. Hosea (American Institute of Physics Conference Proceedings), No. 289, p.72.

[8] D. Grove, V. Arunasalam, K. Bol, D. Boyd, N. Bretz, M. Brusati, S. Cohen, D. Dimock, F. Dylla, D. Eames, H. Eubank, B. Fraenkel, J. Girard, R. Hawryluck, E. Hinnov, R. Horton, J. Hosea, H. Hsuan, D. Ignat, F. Jobes, D. Johnson, E. Mazzucato, E. Meservey, N. Sauthoff, *Plasma Physics and*

Controlled Nuclear Fusion Research, 1976, (Internatinal Atomic Energy Agency, Vienna 1977), Vol. I, p. 21.

[9]M. Porkolab, J.J. Schuss, Y. Takase, S. Knowlton, S.C. Luckhardt, R.E. Slusher, C.M. Surko, N.J. Fisch, W.M. Hooke, C.F.F. Karney, A.H. Kritz, R. McWilliams, R.W. Motley, M. Ono, F.W. Perkins, T.H. Stix, E.J. Valeo, J.R. Wilson, K.-L. Wong, *Plasma Physics and Controlled Nuclear Fusion Research, 1980,* (International Atomic Energy Agency, Vienna, 1981), Vol. II, p. 507.

[10]M. Ono, P. Beiersdorfer, R. Bell, S. Bernabei, A. Cavallo, A. Chmyga, S. Cohen, P. Colestock, G. Gammel, G.J. Greene, J. Hosea, R. Kaita, I. Lehrman, G. Mazzitelli, E. Mazzucato, D. McNeill, K. Sato, J. Stevens, J. Timberlake, J.R. Wilson, and A. Wousters, Phys. Rev. Lett. **60**, 294 (1988).

[11]J.D. Moody, M. Porkolab, C.L. Fiore, F.S. McDermott, Y. Takase, J. Terry, S.M. Wolfe, Phys. Rev. Lett. **60**, 298 (1988)

[12]T. Seki, R. Kumazawa, T. Watari, M. Ono, Y. Yasaka, F. Shimpo, A. Ando, O. Kaneko, Y. Oka, K. Adati, R. Akiyama, Y. Hamada, S. Hidekuma, S. Hirokura, K. Ida, A. Karita, K. Kawahata, T. Kawamoto, Y. Kawasumi, Y. Kitoh, M. Kojima, K. Masai, S. Morita, K. Narihara, Y. Ogawa, K. OHkubo, S. Okajima, T. Ozaki, M. Sakamoto, M. Sasao, K. Sato, K.N. Sato, H. Takahashi, Y. Taniguchi, K. Toi, T. Tsuzuki, Nuclear Fusion **32**, 2189 (1992).

[13]B. LeBlanc, M. Ono, W. Tighe, J. Dunlap, R. Bell, T.K. Chu, A. England, R. Isler, S. Kaye, D. McCune, M. Okabayashi, A. Post-Zwicker, H. Takahashi, S. Sesnic, *Radio Frequency Power in Plasmas, 10th Topical Conference, Boston, MA, 1993,* edited by M. Porkolab and J. Hosea (American Institute of Physics Conference Proceedings), No. 289, 1993, p.68

---

[14]Would Survey of Activities in Controlled Fusion Research, Special Supplement of Nuclear Fusion, p.195 (1991)

[15]S. Sesnic, J. Dunlap, R. Kaita, S.M. Kaye, M. Okabayashi, to be published in Plasma Physics and Controlled Fusion

[16]B. LeBlanc, R. Bell, D. Dimock, P.-A. Duperrex, J. Felt, R. Palladino, E. Tolnas, Rev. Sci. Instrum. **61**, 3566 (1990).

[17]R.J. Hawryluk, in Physics of Plasma Close to Thermonuclear Conditions, International School of Plasma Physics, (Proc. of Course held in Varenna, Italy, 1979), Vol 1, p.19, Commission of the European Communities, Brussels, 1980

[18]R.J. Goldston, D.C. McCune, H.H. Towner, S.L. Davis, R.J. Hawryluk, G.L. Schmidt, J. Comp. Phys. **43**, 61 (1981)

[19]B. LeBlanc, S. Kaye, N. Asakura R. Bell, P. Duperrex, G. Gammel, H. Fishman, R. Hatcher, A. Holland, R. Kaita, C. Kessel, H. Kugel, F. Levinton, M. Okabayashi. S. Paul, N. Sauthoff, S. Sesnic, H. Takahashi, Nuclear Fusion, **33**, 1645 (1993).

[20]A. A. Ware, Phys. Rev. Lett. **25**, 15 (1970).

[21]"Impurity Behavior During Ion Bernstein Wave Heating in the PBX-M Tokamak" by Post Zwicker, Isler, Tighe, Paul, Ono, LeBlanc, Bell, and Kugel, submitter to Nuclear Fusion

[22]C. E. Kessel, computer code FQ (Plasma Physics Laboratory, Princeton, NJ, 1989)

or

C.E. Kessel, F. Hofmann, S.C. Jardin, R. Kaita, F. Levinton and M. Okabayashi, Bulletin of the American Physical Society **34**, 2050 (1989).

[23] A.C. England, R. Kaita, H.W. Kugel, and H.J. Oliver, PPPL-TM-400, Plasma Physics Laboratory, Princeton University, 1993

[24] A. M. Zolfaghari, S. Luckhardt, P. P. Woskov, D. R. Cohn, S. Jones, J. Kesner, J. Machuzak, J. Ramos, D. V. Bartlett, A. E. Costley, P. Cripwell, L. Porte, R. J. Smith, and R. Kaita, Rev. of Sci. Instrum. **63**, 4619 (1992).

[25] H. Biglari, M. Ono, P.H. Diamond, G.G. Graddock, *Radio-Frequency Power in Plasmas, 9th Topical Conference, Charleston, 1991,* edited by D.B. Batcheler (American Institute of Physics Conference Proceedings), No. 244, 1992, p.376.

[26] H. Biglari, P.H. Diamond, P.W. Terry, Phys. Fluids B **2,** 1 (1990).

[27] E.A. Lazarus, J.D. Bell, C.E. Bush, A. Carnevali, B.A. Carreras, W.H. Casson, J.L. Dunlap, PH. Edmonds, A.C. England, W.L. Gardner, G.A. Hallock, J.T. Hogan, H.C. Howe, D.P. Hutchinson, R.R. Kindsfather, R.C. Isler, R.A. Langley, C.H. Ma, J. Matthew, P.K. Mioduszewski, M. Murakami, G.H. Neilson, V.K. Pare, D.J. Sigmar, C.E. Thomas, R.M. Wieland, J.B. Wilgen, W.R. Wing, A.J. Wootton, K.E. Yokoyama, Nucl. Fusion. **25**, 135 (1985).

[28] D.W. Swain, M. Murakami, S.C. Bates, C.E. Bush, J.L. Dunlap, P.H. Edmonds, D. Hutchinson, P.W. King, E.A. Lazarus, J.F. Lyon, C.H. Ma, J.T. Mihalczo, L.E. Murray, G.H. Neilson, V.K. Pare, M.J. Saltmarsh, S.D. Scott, C.E. Thomas, J.R. Wilgen, R.M. Wieland, Nucl. Fusion. **21**, 1409 (1981).

[29] G.H. Wolf, J. Nucl. Mater. **122&123**, 1124 (1984).

[30] J. Winter, H.G. Esser, G.L. Jackson, L. Konen, A. Messiaen, J. Ongena, V. Philipps, A. Pospieszczyk,, U. Samm, B. Unterberg, and the TEXTOR team, Phys. Rev. Lett. **71**, 1549 (1993).

FIGURE CAPTIONS

Fig. 1: Time evolution overlay for NBI discharges: (black) with sustained IBWH, (gray) with short IBWH pulse. From *top to bottom*: n_{el}, the line integrated density; I_{Xo}, soft x ray signal at plasma center; $I_{Xa/2}$, soft x-ray signal at $r/a=1/2$; D_α, deuterium line intensity at 0.656 μm; IBW power.

Fig. 2: Time evolution overlay for IBWH-assisted and NBI-only discharges: *Top panel:* Neutron source strength S_n; for times greater than 0.595 s, the IBWH-assisted discharge enters the CH-mode and S_n recovers. *Second panel:* Time evolution of T_{io}; recovery happens simultaneously with S_n. *Third panel:* Total stored energy W_{tot} obtained from TRANSP analyses; recovery is also observed.

Fig. 3: *Top:* Overlay of a sequence of electron density profiles for discharges with IBWH-assisted discharge with IBWH starting at 0.46 s. *Middle:* Density peaking parameter $n_{eo}/<n_e>$ against time; data derived from Thomson scattering measurements. *Bottom:* T_{eo} time evolution extracted from concatenation of Thomson scattering data. Experimental points: open squares; smoothed curve: solid line. Typical experimental error bars shown. Time evolution of n_{eo} against time.

Fig. 4: Profiles of T_e, n_e, ∇T_e and ∇n_e : IBWH assisted NBI (black) and NBI only (gray) discharges. The IBWH data correspond to CH-mode phase. The NBI only data correspond to an ELMing H-mode. Compared to the H-mode discharge, the confinement zone of the CH-mode is moved inward.

Fig. 5: Profiles of T_i, v_ϕ, ∇T_i and ∇v_ϕ during CH-mode and equivalent time during NBI-only discharge.

Fig. 6: ELM induced soft x-ray loss profiles: *top*, NBI only discharge; *bottom*, IBWH assisted NBI discharge. Localized minima of the soft x-ray loss are seen with IBWH operation.

Fig. 7: Ion thermal diffusivity, χ_i, momentum diffusivity, χ_ϕ, and electron thermal diffusivity, χ_{er} (including radiative effects), against time. Volume average over $0.3 < r/a < 0.45$. L-H transition occurs ≈0.42 s, followed by H-mode. CH-mode development begins at ≈0.60 s; saturated CH-mode for times greater than 0.65 s.

Fig. 8: Electron particle diffusivity D_e during CH-mode at 0.65 s. Computation made for no pinch, 1x Ware and 5x Ware pinch velocity.

Fig. 9: Comparison of TRANSP output with measurements. *Top:* time evolution of stored energy from TRANSP using Z_{eff} from visible continuum (Z_{eff}(VC)) and from surface voltage ($Z_{eff}(V_{sur})$), for variable and/or constant Z_I; magnetically derived W_{tot} at individual time points (FQ equilibrium code)). Reasonable agreement is obtained for the impurity modeling shown. *Bottom:* TRANSP calculations of S_n using same impurity modelings as above, and measurement (EXP). Temporal agreement is obtained with Z_{eff}(Vsur).

Fig. 10: Enhanced core heating: IBWH assisted discharge in black, NBI only reference discharge in gray. *Top panel:* auxiliary heating against time. *Bottom panel:* S_n against time. A 60% increase in neutron production is obtained through a modest addition of IBWH power (less than 10% of total input power.)

Fig. 11: Bootstrap current, from TRANSP, during enhanced core heating discharge for different Z_I assumptions. *Top panel:* j_{BS}/j at r/a=1/2 against time. *Bottom panel:* profile of the bootstrap, j_{BS}, the beam driven, j_{BD}, and the total current, j, at 0.64 s. j_{BS}/j ranges from 0.32 to 0.35 depending on Z_I assumption (variable or constant).

Fig. 12: Enhanced core heating: Ion thermal diffusivity, χ_i, momentum diffusivity, χ_ϕ, and electron thermal diffusivity, χ_{er} (including radiative effects), against time. Volume average over $0.3 < r/a < 0.45$. L-H transition occurs at ≈0.45 s, followed by short H-mode phase. Nominal onset of CH-mode development at 0.56 s; CH-mode fully developed for times greater than 0.65 s. Auxiliary power can be read on right vertical axis. CH-mode confinement is maintained during NBI core heating burst starting at 0.55 s.

Fig. 13: Spatial correlation of transport barrier features, with P_{IBWH}. Mapping of ∇n_e, ∇T_e, ∇v_ϕ, ∇T_i ,and P_{IBWH} against R. Arrows indicate locations of transport of Δ_{Ix} minima as projected onto R. Location of q=3/2 surface is also shown.

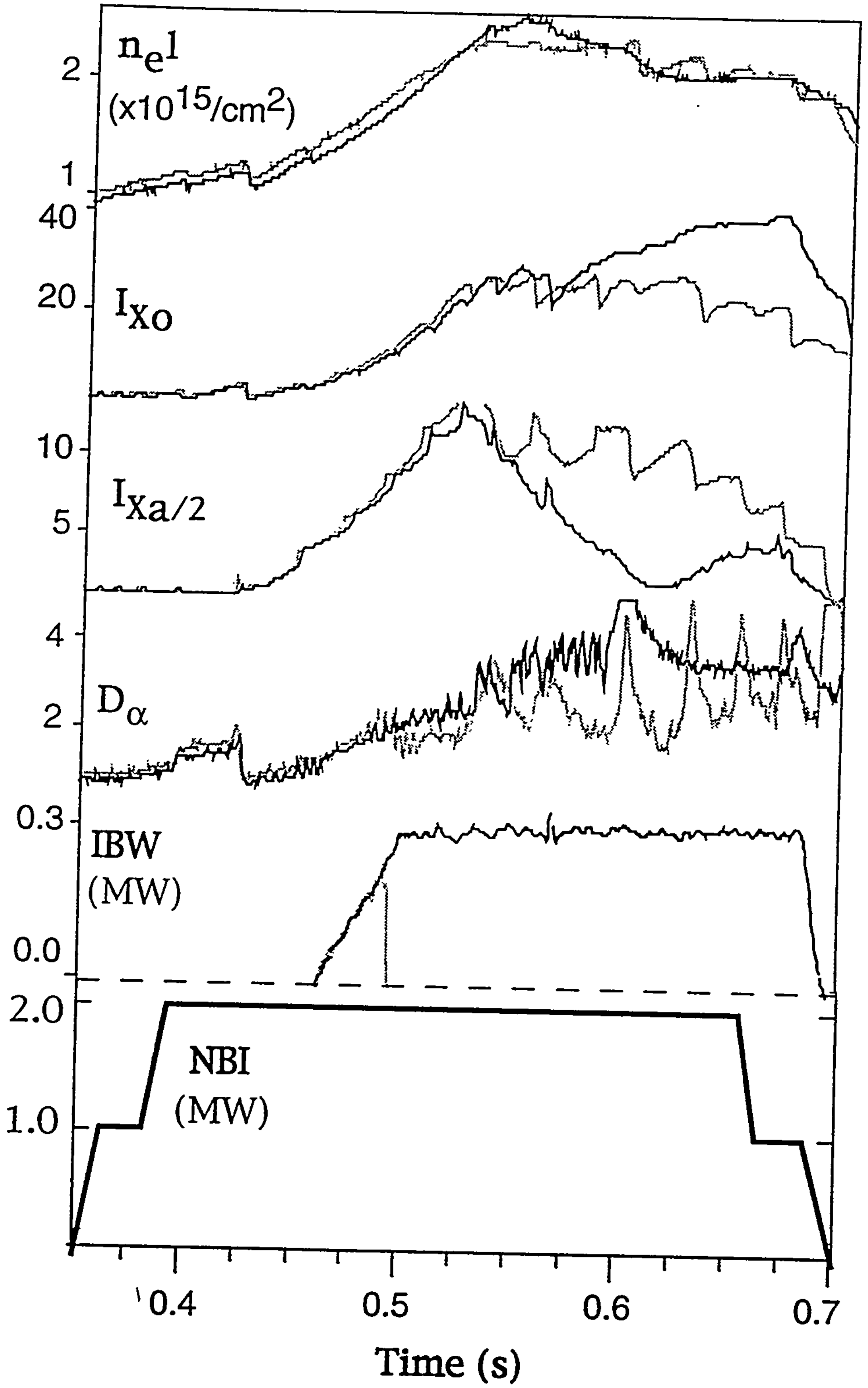

$n_e l$
$(\times 10^{15}/cm^2)$
2
1
40
20
I_{Xo}
10
5
$I_{Xa/2}$
4
2
D_α
0.3
IBW
(MW)
0.0
2.0
1.0
NBI
(MW)
0.4
0.5
0.6
0.7
Time (s)

Fig. 1

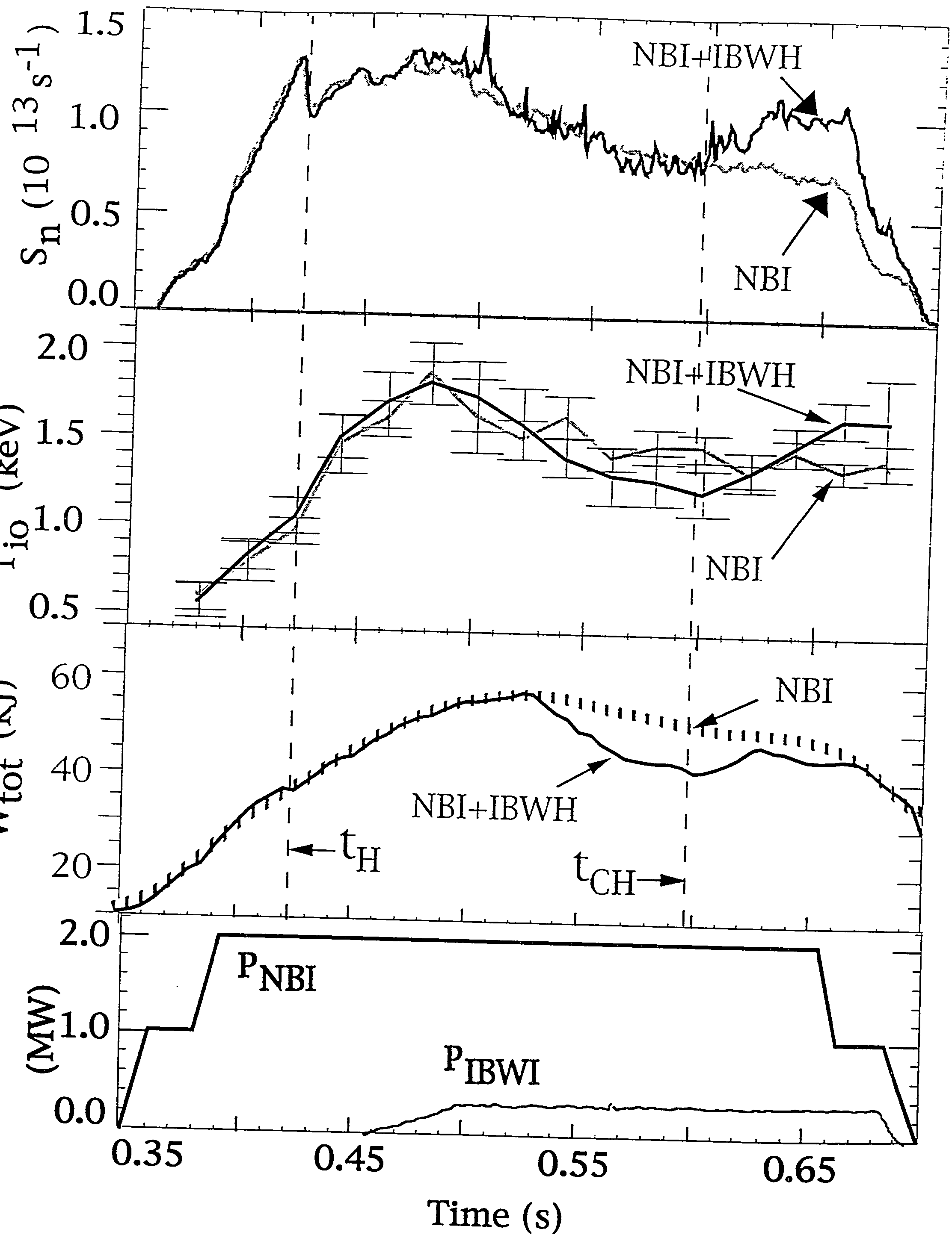

S_n (10 ^{13} s^{-1})
1.5
1.0
0.5
0.0
NBI+IBWH
NBI
T_{io} (keV)
2.0
1.5
1.0
0.5
NBI+IBWH
NBI
W_{tot} (kJ)
60
40
20
NBI
NBI+IBWH
t_H
t_{CH}
(MW)
2.0
1.0
0.0
P_{NBI}
P_{IBWI}
0.35
0.45
0.55
0.65
Time (s)

Fig. 2

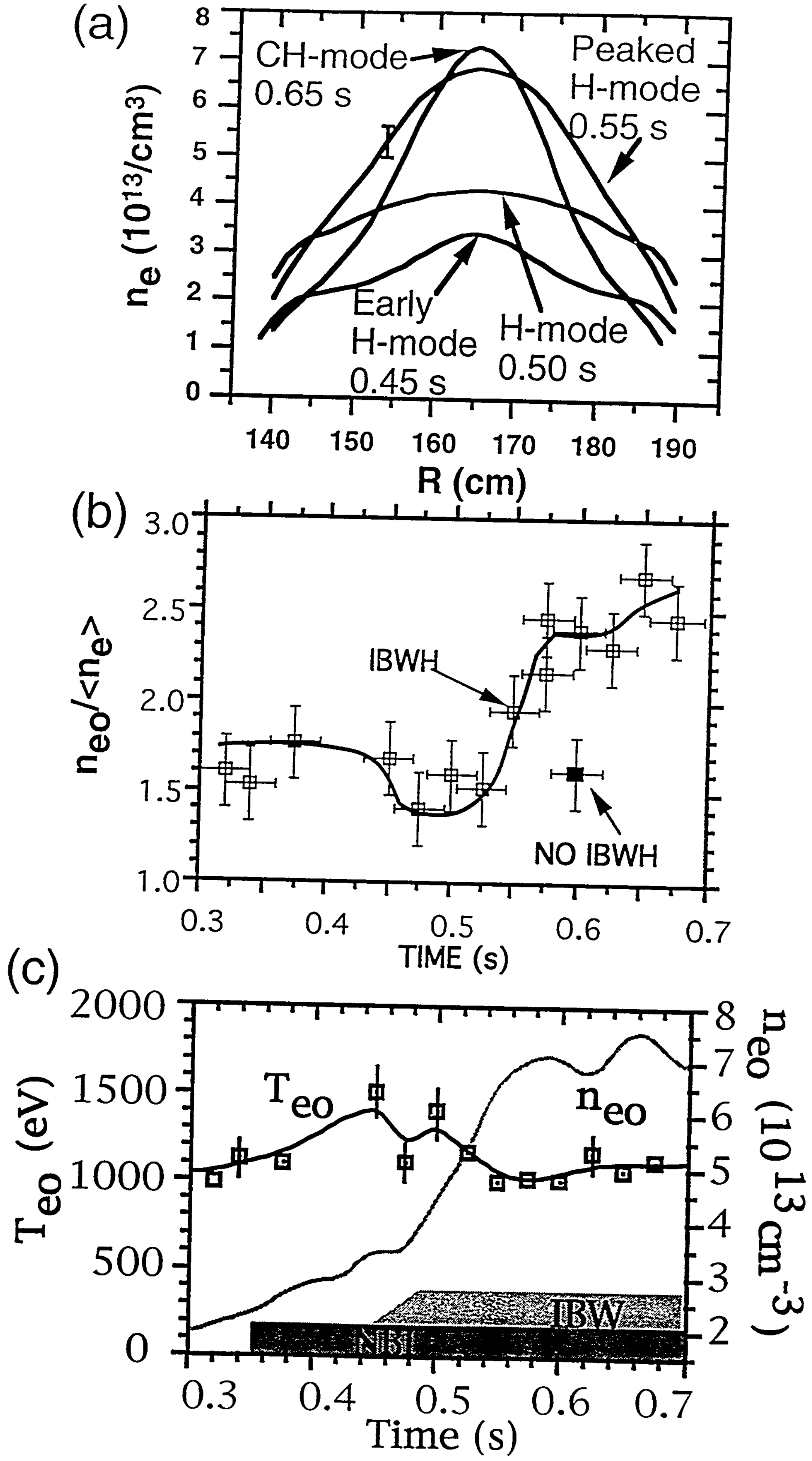
(a)
n_e (10^{13}/cm^3)
R (cm)
CH-mode 0.65 s
Peaked H-mode 0.55 s
Early H-mode 0.45 s
H-mode 0.50 s
0
1
2
3
4
5
6
7
8
140
150
160
170
180
190
(b)
$n_{eo}/\langle n_e \rangle$
TIME (s)
IBWH
NO IBWH
1.0
1.5
2.0
2.5
3.0
0.3
0.4
0.5
0.6
0.7
(c)
T_{eo} (eV)
n_{eo} (10^{13} cm^{-3})
Time (s)
T_{eo}
n_{eo}
IBW
NBI
0
500
1000
1500
2000
2
3
4
5
6
7
8
0.3
0.4
0.5
0.6
0.7

Fig. 3

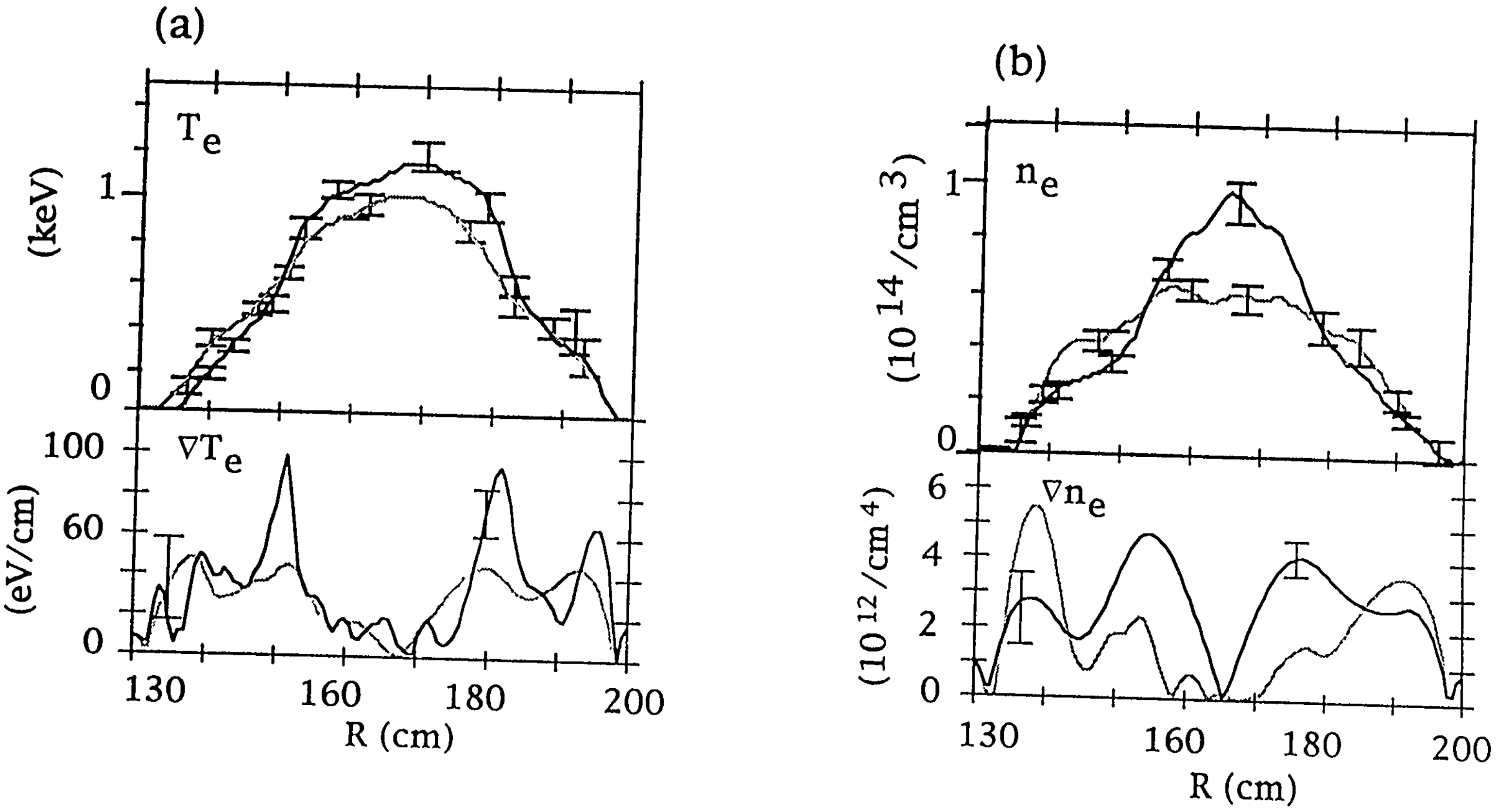
(a)
T_e
(keV)
1
0
∇T_e
(eV/cm)
100
60
0
130
160
180
200
R (cm)
(b)
n_e
(10 14/cm 3)
1
0
∇n_e
(10 12/cm 4)
6
4
2
0
130
160
180
200
R (cm)

Fig. 4

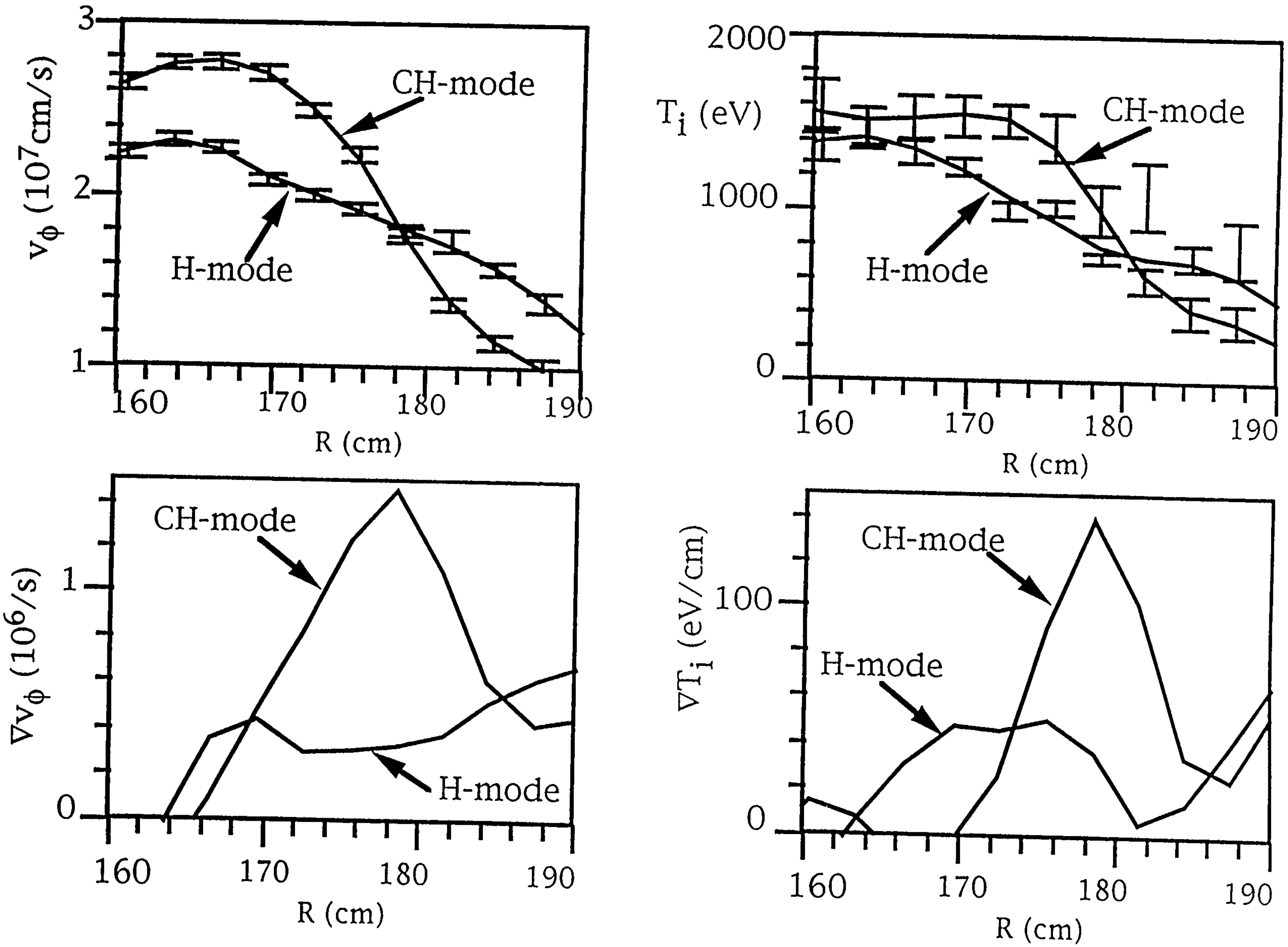
3
2
1
v_ϕ (10^7cm/s)
CH-mode
H-mode
160
170
180
190
R (cm)
2000
1000
0
T_i (eV)
CH-mode
H-mode
160
170
180
190
R (cm)
1
0
∇v_ϕ (10^6/s)
CH-mode
H-mode
160
170
180
190
R (cm)
100
0
∇T_i (eV/cm)
CH-mode
H-mode
160
170
180
190
R (cm)

Fig. 5

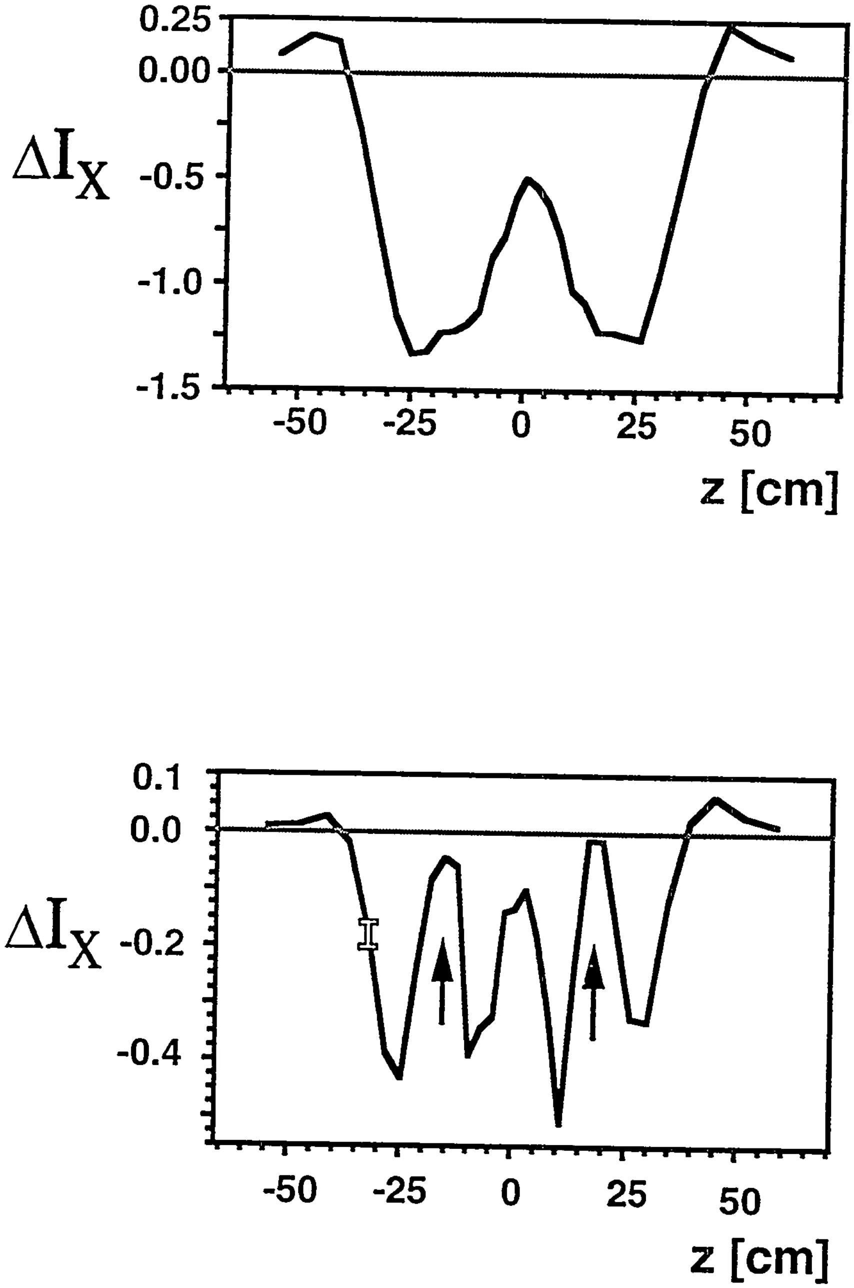
0.25
0.00
ΔI_X
-0.5
-1.0
-1.5
-50
-25
0
25
50
z [cm]
0.1
0.0
ΔI_X
-0.2
-0.4
-50
-25
0
25
50
z [cm]

Fig. 6

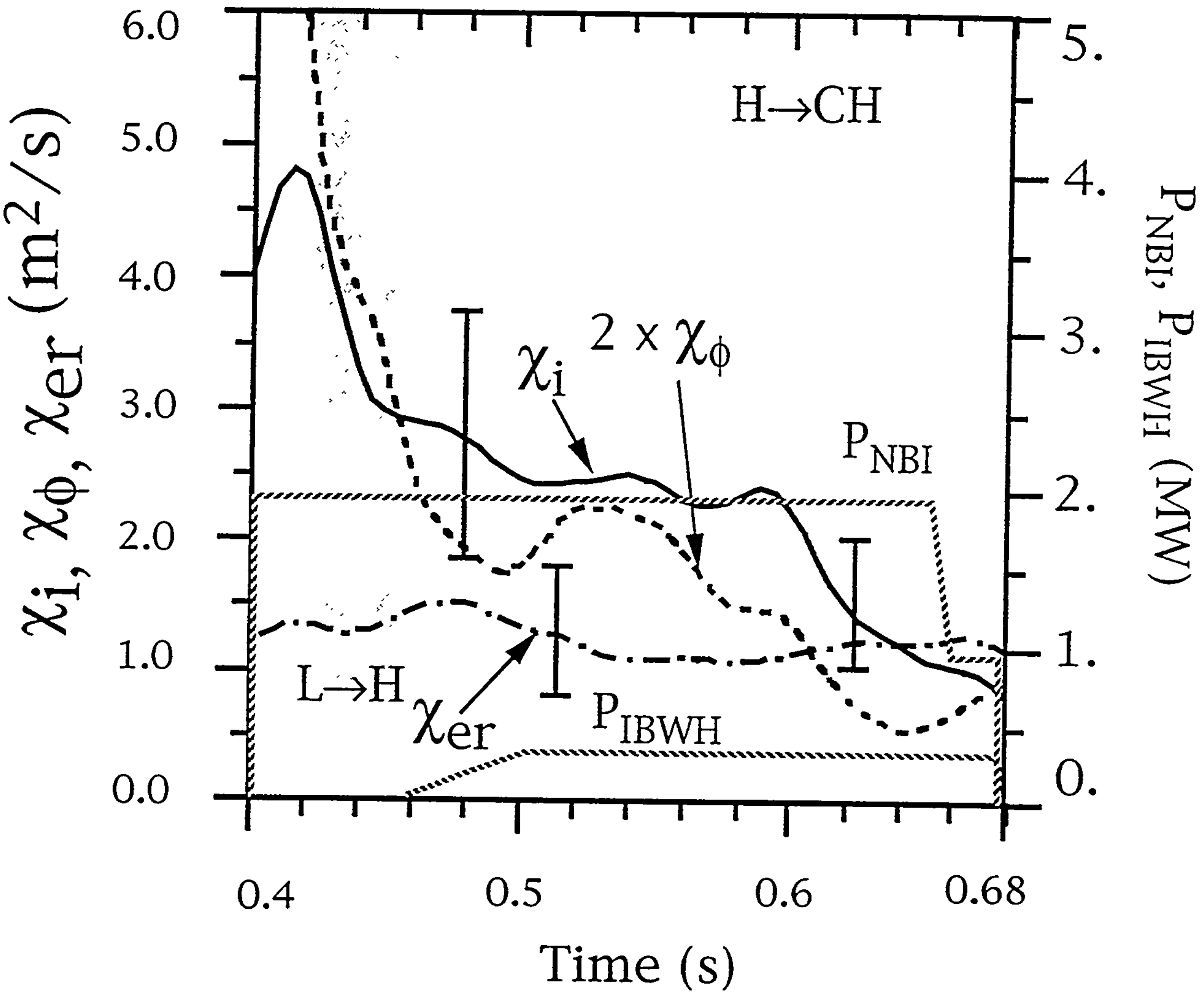

χ_i, χ_ϕ, χ_{er} (m^2/s)
6.0
5.0
4.0
3.0
2.0
1.0
0.0
H→CH
χ_i
2 x χ_ϕ
P_{NBI}
L→H
χ_{er}
P_{IBWH}
5.
4.
3.
2.
1.
0.
P_{NBI}, P_{IBWH} (MW)
0.4
0.5
0.6
0.68
Time (s)

Fig. 7

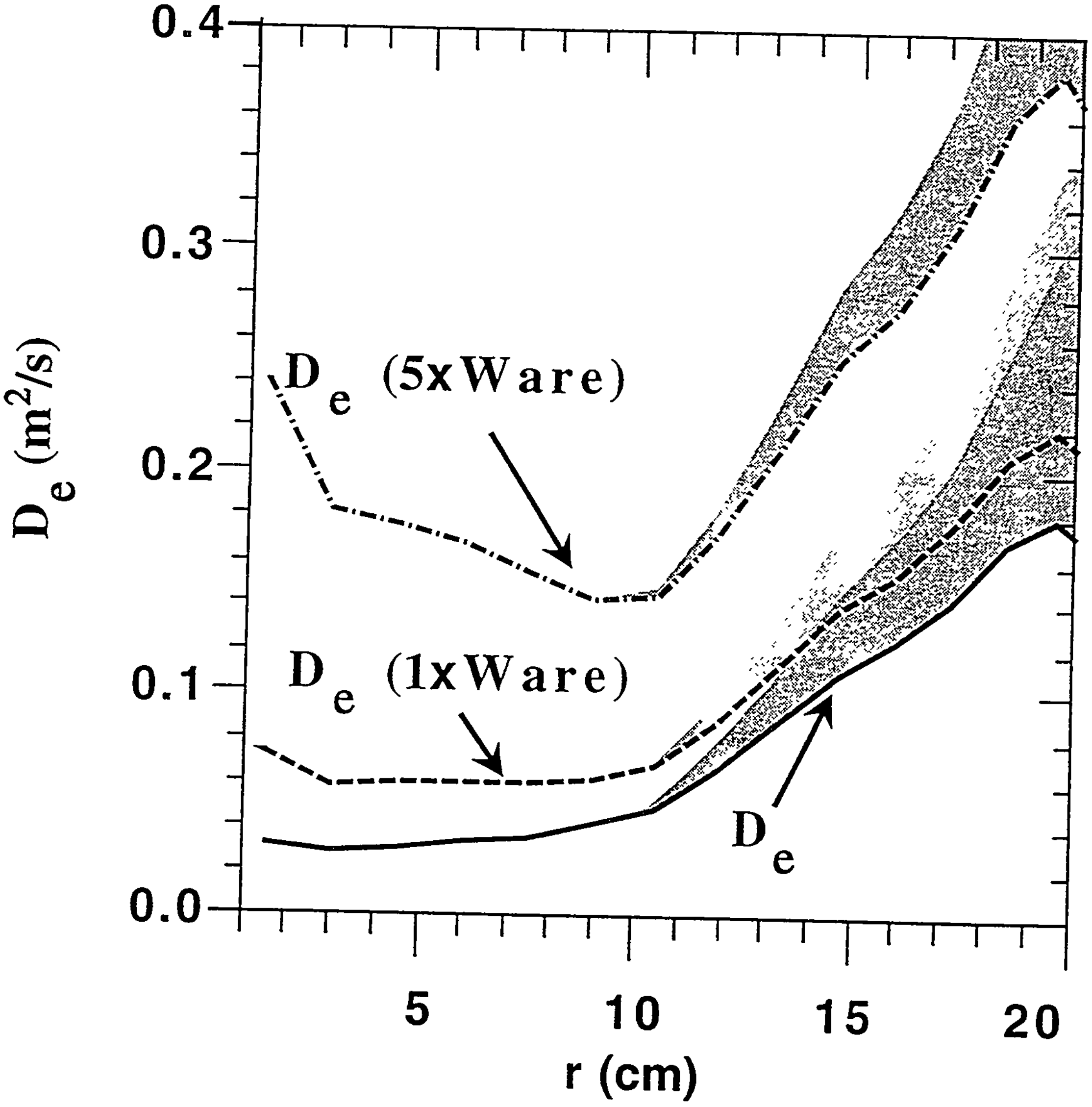

Fig. 8

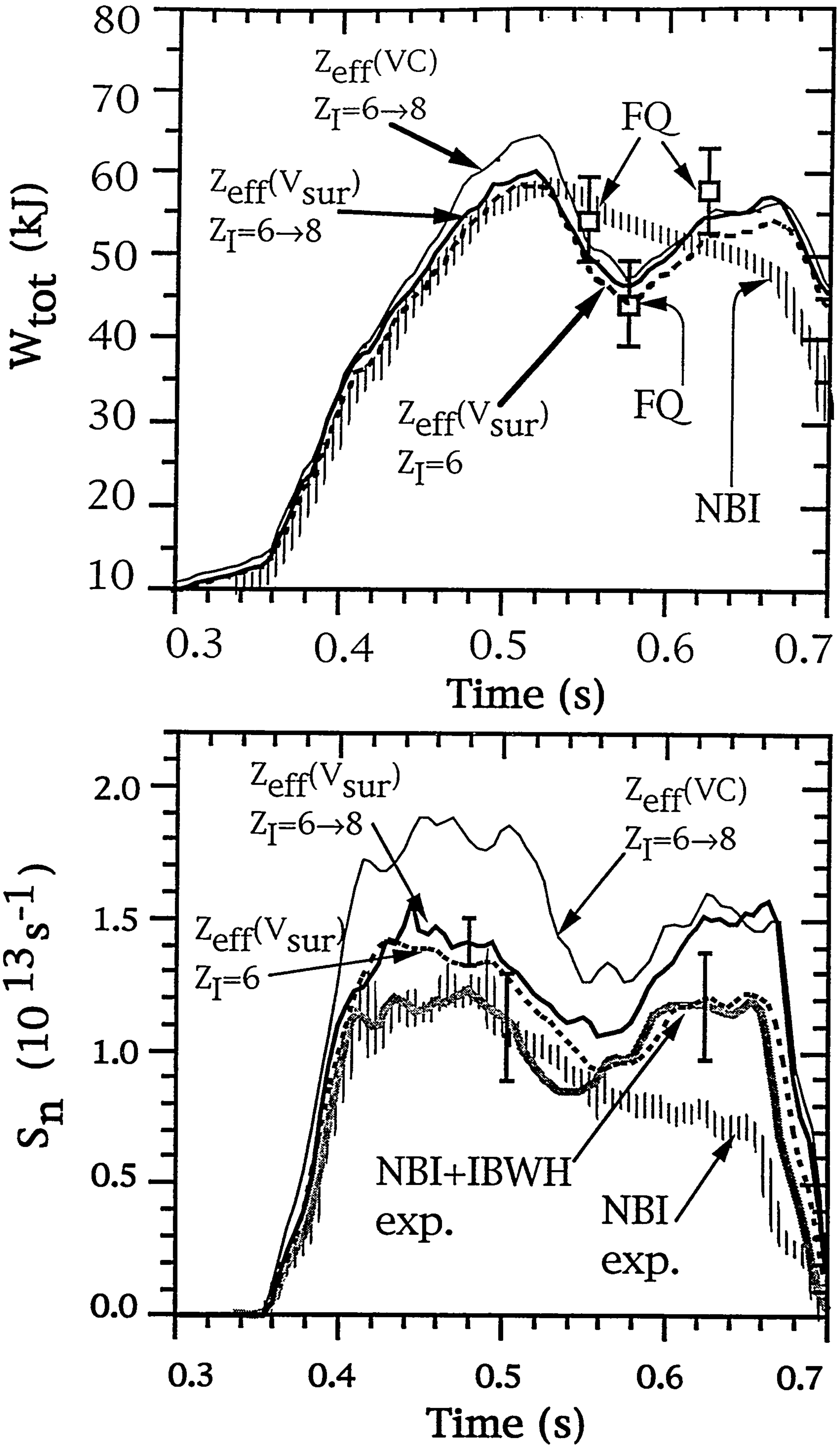

W_{tot} (kJ)
80
70
60
50
40
30
20
10
Z_{eff}(VC) Z_I=6→8
Z_{eff}(V_{sur}) Z_I=6→8
FQ
FQ
Z_{eff}(V_{sur}) Z_I=6
NBI
0.3
0.4
0.5
0.6
0.7
Time (s)
S_n ($10^{13}s^{-1}$)
2.0
1.5
1.0
0.5
0.0
Z_{eff}(V_{sur}) Z_I=6→8
Z_{eff}(VC) Z_I=6→8
Z_{eff}(V_{sur}) Z_I=6
NBI+IBWH exp.
NBI exp.
0.3
0.4
0.5
0.6
0.7
Time (s)

Fig. 9

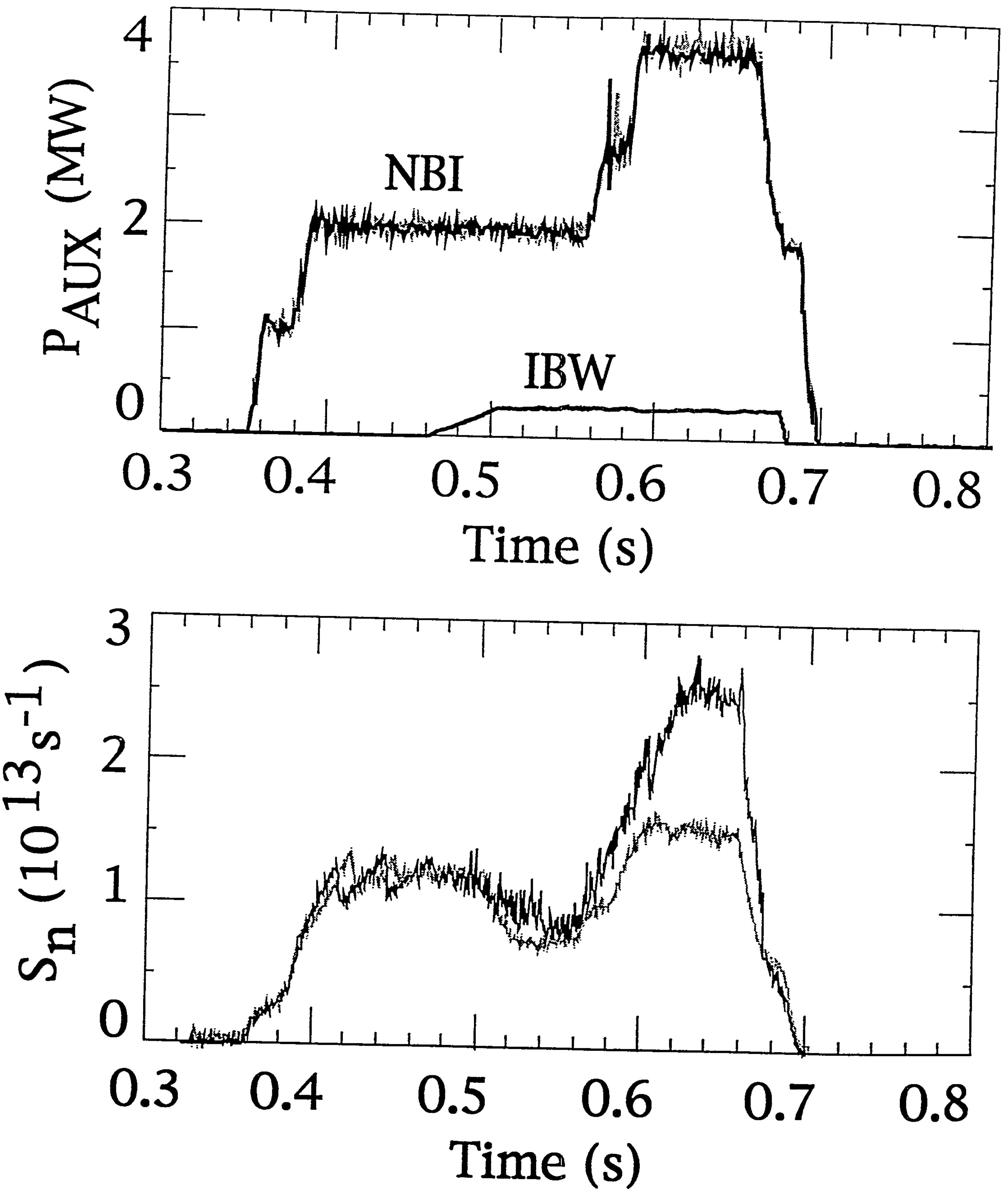

P_AUX (MW)
4
2
0
NBI
IBW
0.3
0.4
0.5
0.6
0.7
0.8
Time (s)
S_n (10^13 s^-1)
3
2
1
0
0.3
0.4
0.5
0.6
0.7
0.8
Time (s)

Fig. 10

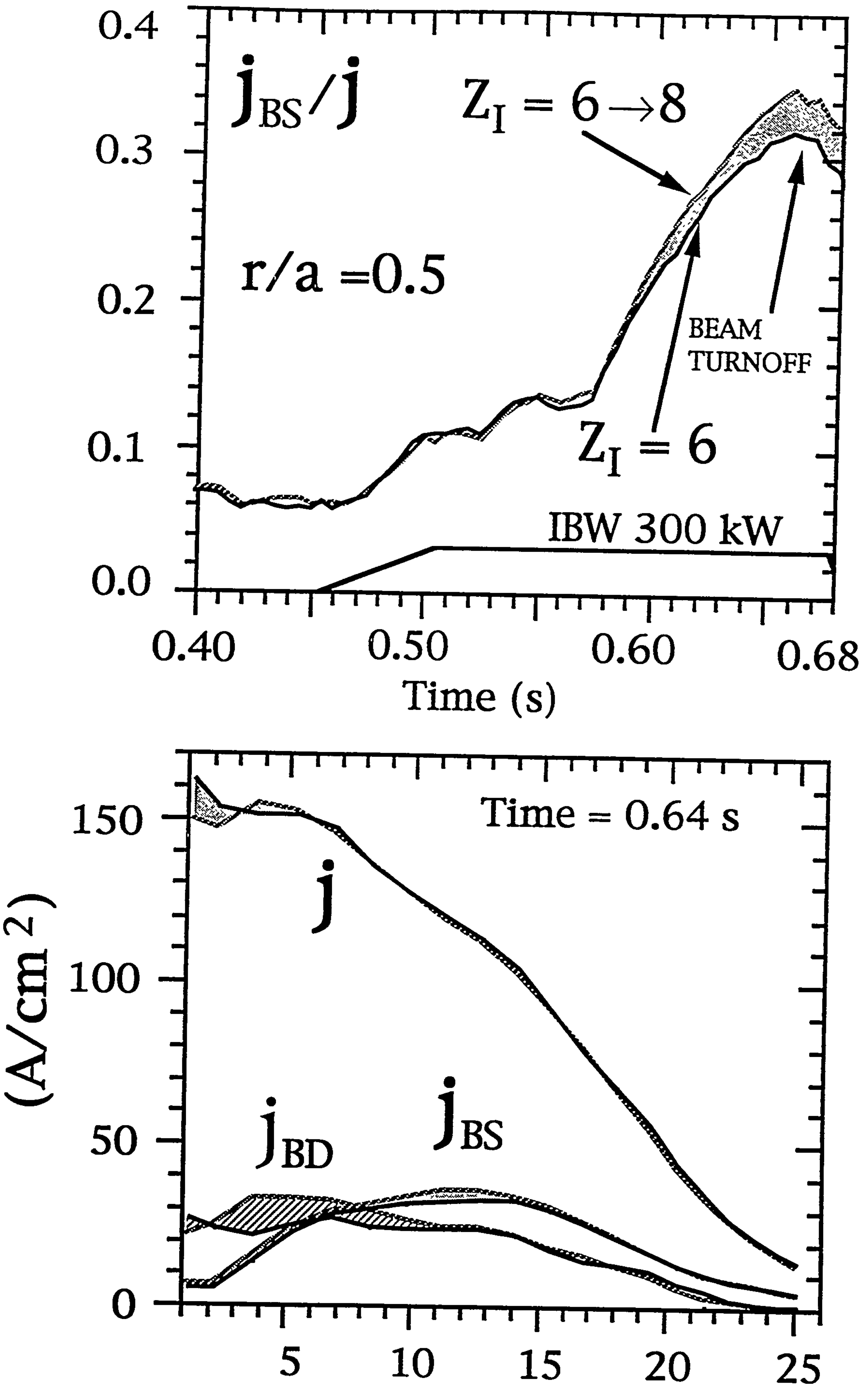
0.4
0.3
0.2
0.1
0.0
j_{BS}/j
$Z_I = 6 \rightarrow 8$
r/a =0.5
BEAM TURNOFF
$Z_I = 6$
IBW 300 kW
0.40
0.50
0.60
0.68
Time (s)
150
100
50
0
(A/cm^2)
Time = 0.64 s
j
j_{BD}
j_{BS}
5
10
15
20
25
r (cm)

Fig. 11

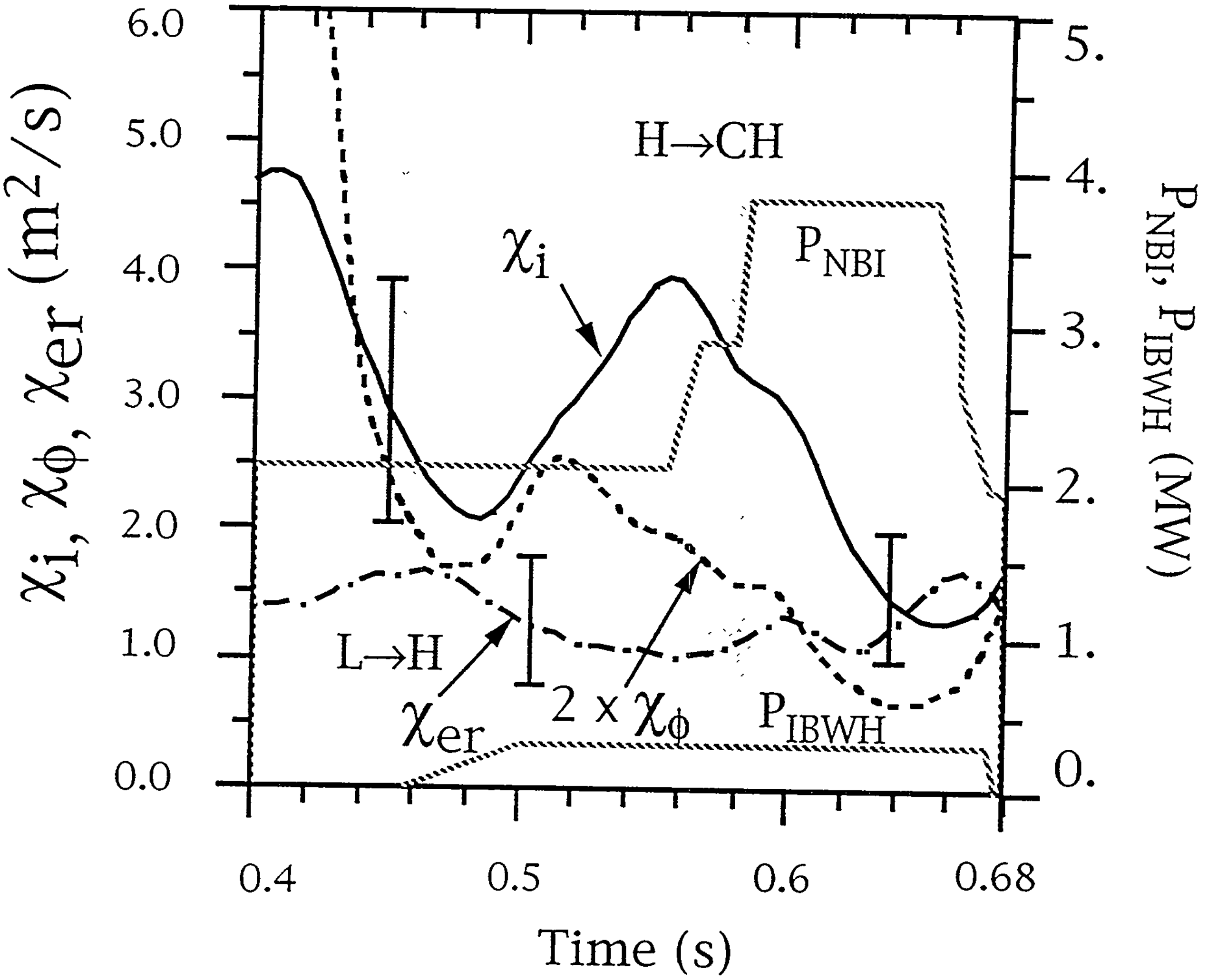
6.0
5.0
4.0
3.0
2.0
1.0
0.0
χ_i, χ_ϕ, χ_{er} (m^2/s)
5.
4.
3.
2.
1.
0.
P_{NBI}, P_{IBWH} (MW)
H→CH
χ_i
P_{NBI}
L→H
χ_{er}
2 x χ_ϕ
P_{IBWH}
0.4
0.5
0.6
0.68
Time (s)

Fig. 12

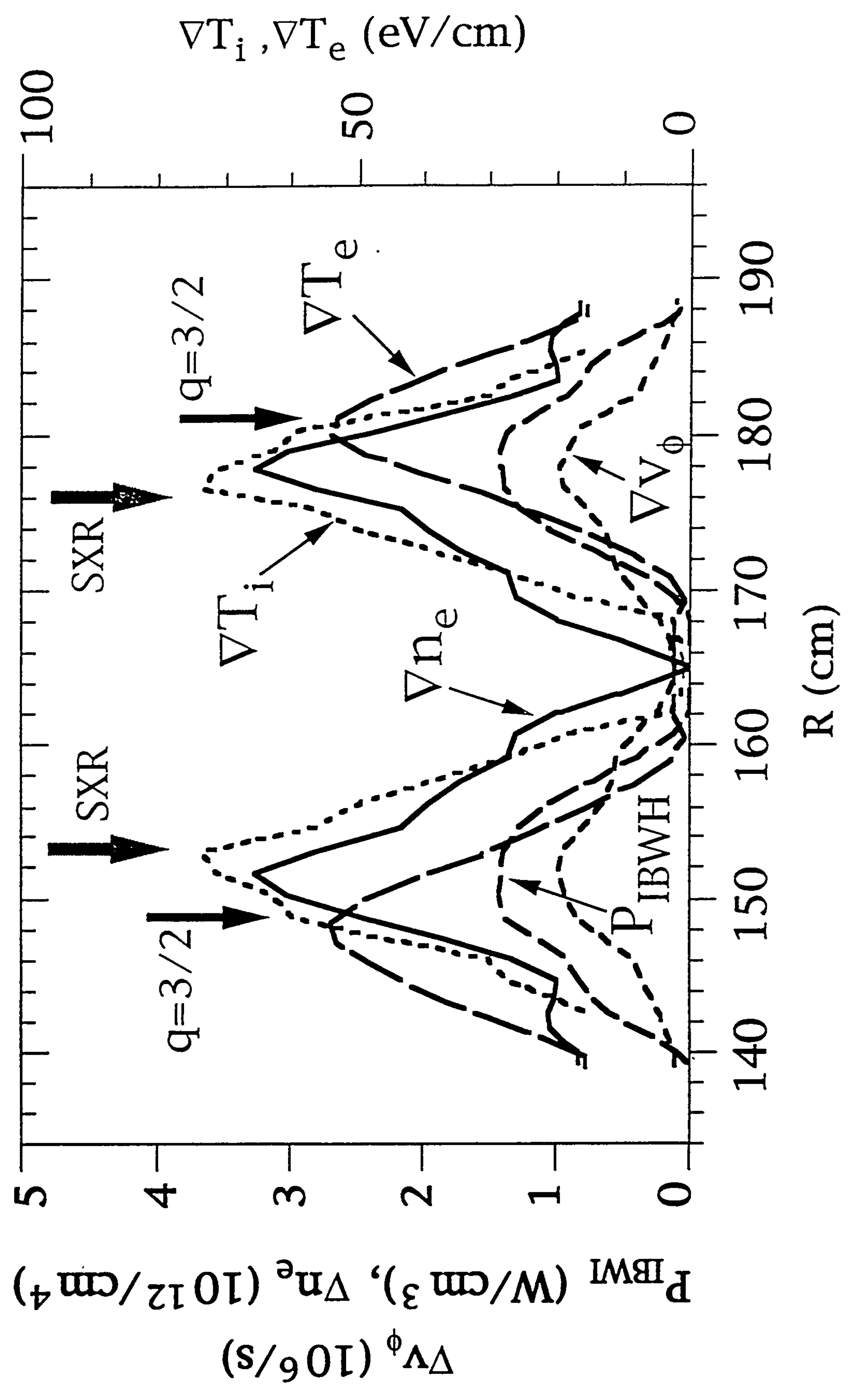

$\nabla T_i, \nabla T_e$ (eV/cm)
100
50
0
∇T_e
q=3/2
SXR
∇T_i
∇n_e
∇v_ϕ
SXR
q=3/2
P_{IBWH}
140
150
160
170
180
190
R (cm)
5
4
3
2
1
0
P_{IBWH} (W/cm^3), ∇n_e (10^{12}/cm^4)
∇v_ϕ (10^6/s)

Fig. 13

EXTERNAL DISTRIBUTION IN ADDITION TO UC-420

Dr. F. Paoloni, Univ. of Wollongong, AUSTRALIA
Prof. R.C. Cross, Univ. of Sydney, AUSTRALIA
Plasma Research Lab., Australian Nat. Univ., AUSTRALIA
Prof. I.R. Jones, Flinders Univ, AUSTRALIA
Prof. F. Cap, Inst. for Theoretical Physics, AUSTRIA
Prof. M. Heindler, Institut für Theoretische Physik, AUSTRIA
Prof. M. Goossens, Astronomisch Instituut, BELGIUM
Ecole Royale Militaire, Lab. de Phy. Plasmas, BELGIUM
Commission-European, DG. XII-Fusion Prog., BELGIUM
Prof. R. Boucique, Rijksuniversiteit Gent, BELGIUM
Dr. P.H. Sakanaka, Instituto Fisica, BRAZIL
Prof. Dr. I.C. Nascimento, Instituto Fisica, Sao Paulo, BRAZIL
Instituto Nacional De Pesquisas Espaciais-INPE, BRAZIL
Documents Office, Atomic Energy of Canada Ltd., CANADA
Ms. M. Morin, CCFM/Tokamak de Varennes, CANADA
Dr. M.P. Bachynski, MPB Technologies, Inc., CANADA
Dr. H.M. Skarsgard, Univ. of Saskatchewan, CANADA
Prof. J. Teichmann, Univ. of Montreal, CANADA
Prof. S.R. Sreenivasan, Univ. of Calgary, CANADA
Prof. T.W. Johnston, INRS-Energie, CANADA
Dr. R. Bolton, Centre canadien de fusion magnétique, CANADA
Dr. C.R. James,, Univ. of Alberta, CANADA
Dr. P. Lukác, Komenského Universzita, CZECHO-SLOVAKIA
The Librarian, Culham Laboratory, ENGLAND
Library, R61, Rutherford Appleton Laboratory, ENGLAND
Mrs. S.A. Hutchinson, JET Library, ENGLAND
Dr. S.C. Sharma, Univ. of South Pacific, FIJI ISLANDS
P. Mähönen, Univ. of Helsinki, FINLAND
Prof. M.N. Bussac, Ecole Polytechnique,, FRANCE
C. Mouttet, Lab. de Physique des Milieux Ionisés, FRANCE
J. Radet, CEN/CADARACHE - Bat 506, FRANCE
Prof. E. Economou, Univ. of Crete, GREECE
Ms. C. Rinni, Univ. of Ioannina, GREECE
Preprint Library, Hungarian Academy of Sci., HUNGARY
Dr. B. DasGupta, Saha Inst. of Nuclear Physics, INDIA
Dr. P. Kaw, Inst. for Plasma Research, INDIA
Dr. P. Rosenau, Israel Inst. of Technology, ISRAEL
Librarian, International Center for Theo Physics, ITALY
Miss C. De Palo, Associazione EURATOM-ENEA , ITALY
Dr. G. Grosso, Istituto di Fisica del Plasma, ITALY
Prof. G. Rostangni, Istituto Gas Ionizzati Del Cnr, ITALY
Dr. H. Yamato, Toshiba Res & Devel Center, JAPAN
Prof. I. Kawakami, Hiroshima Univ., JAPAN
Prof. K. Nishikawa, Hiroshima Univ., JAPAN
Librarian, Naka Fusion Research Establishment, JAERI, JAPAN
Director, Japan Atomic Energy Research Inst., JAPAN
Prof. S. Itoh, Kyushu Univ., JAPAN
Research Info. Ctr., National Instit. for Fusion Science, JAPAN
Prof. S. Tanaka, Kyoto Univ., JAPAN
Library, Kyoto Univ., JAPAN
Prof. N. Inoue, Univ. of Tokyo, JAPAN
Secretary, Plasma Section, Electrotechnical Lab., JAPAN
Dr. O. Mitarai, Kumamoto Inst. of Technology, JAPAN
Dr. G.S. Lee, Korea Basic Sci. Ctr., KOREA
J. Hyeon-Sook, Korea Atomic Energy Research Inst., KOREA
D.I. Choi, The Korea Adv. Inst. of Sci. & Tech., KOREA
Prof. B.S. Liley, Univ. of Waikato, NEW ZEALAND
Inst of Physics, Chinese Acad Sci PEOPLE'S REP. OF CHINA
Library, Inst. of Plasma Physics, PEOPLE'S REP. OF CHINA
Tsinghua Univ. Library, PEOPLE'S REPUBLIC OF CHINA
Z. Li, S.W. Inst Physics, PEOPLE'S REPUBLIC OF CHINA
Prof. J.A.C. Cabral, Instituto Superior Tecnico, PORTUGAL
Prof. M.A. Hellberg, Univ. of Natal, S. AFRICA
Prof. D.E. Kim, Pohang Inst. of Sci. & Tech., SO. KOREA
Prof. C.I.E.M.A.T, Fusion Division Library, SPAIN
Dr. L. Stenflo, Univ. of UMEA, SWEDEN
Library, Royal Inst. of Technology, SWEDEN
Prof. H. Wilhelmson, Chalmers Univ. of Tech., SWEDEN
Centre Phys. Des Plasmas, Ecole Polytech, SWITZERLAND
Bibliotheek, Inst. Voor Plasma-Fysica, THE NETHERLANDS
Asst. Prof. Dr. S. Cakir, Middle East Tech. Univ., TURKEY
Dr. V.A. Glukhikh,Sci. Res. Inst. Electrophys.I Apparatus, USSR
Dr. D.D. Ryutov, Siberian Branch of Academy of Sci., USSR
Dr. G.A. Eliseev, I.V. Kurchatov Inst., USSR
Librarian, The Ukr.SSR Academy of Sciences, USSR
Dr. L.M. Kovrizhnykh, Inst. of General Physics, USSR
Kernforschungsanlage GmbH, Zentralbibliothek, W. GERMANY
Bibliothek, Inst. Für Plasmaforschung, W. GERMANY
Prof. K. Schindler, Ruhr-Universität Bochum, W. GERMANY
Dr. F. Wagner, (ASDEX), Max-Planck-Institut, W. GERMANY
Librarian, Max-Planck-Institut, W. GERMANY